Ghost orbit spectroscopy

A. S. Bhullar,[1] R. Blümel,[1] and P. M. Koch[2]
[1]*Department of Physics, Wesleyan University, Middletown, Connecticut 06459-0155, USA*
[2]*Department of Physics and Astronomy, Stony Brook University, Stony Brook, New York 11794-3800, USA*
(Received 25 January 2005; published 13 January 2006)

Direct periodic-orbit expansions of individual spectral eigenvalues is a new direction in quantum mechanics. Using a unitary *S*-matrix theory, we present exact, convergent, integral-free ghost orbit expansions of spectral eigenvalues for a step potential in the tunneling regime. We suggest an experiment to extract ghost orbit information from measured spectra in the tunneling regime (ghost orbit spectroscopy). We contrast our unitary, convergent theory with a recently published nonunitary, divergent theory [Yu. Dabaghian and R. Jensen, Eur. J. Phys. **26**, 423 (2005)].

DOI: 10.1103/PhysRevE.73.016211 PACS number(s): 05.45.Mt, 03.65.Ge, 42.25.−p

I. INTRODUCTION

Poincaré emphasized the importance of periodic orbits in classical mechanics [1]. He devoted a chapter of 70 pages (chapter 3) of volume 1 of his monumental work *New Methods of Celestial Mechanics* [1] to an introduction and study of them. Poincaré's fascination with periodic orbits is confirmed by Hadamard, who writes that "No subject held his [Poincaré's] attention more. One could say that he was preoccupied with them all his life." [1].

Gutzwiller recognized the importance of periodic orbits to a quantal treatment of classically chaotic systems [2,3]. Using only $\hbar$ and classical periodic-orbit information such as the topology, action, and stability properties of the periodic orbits [2,3], he was able to calculate the quantum mechanical density of states $\rho(E)$. For a generic quantum system, Gutzwiller's method is not exact. It is a semiclassical theory expected to improve in the limit $\hbar \to 0$.

Though periodic-orbit theory is often associated with approximate, semiclassical theories, for some systems, periodic-orbit theory is exact. Examples are a quantized particle in a space of constant negative curvature [4], Riemann's ζ function [5], and quantum graphs [6,7]. In general, exact periodic-orbit expansions require more than Newtonian periodic orbits. In ray-splitting systems [8–15], wherein system properties change rapidly on the scale of the de Broglie wavelength, an additional class of classical periodic orbits is found to be important. They are called non-Newtonian orbits in Ref. [14].

To illustrate the concept of a non-Newtonian periodic orbit consider the motion of a point particle inside of the "step-in-the-box" potential

$$V_s(x) = \begin{cases} \infty, & \text{for } x \leqslant 0, \\ 0, & \text{for } 0 < x \leqslant a, \\ V_0, & \text{for } a < x < b, \\ \infty, & \text{for } x \geqslant b, \end{cases} \tag{1}$$

shown in Fig. 1. We shall refer to the various periodic orbits shown there. According to Newtonian mechanics, a classical particle with energy $E > V_0$ inside $V_s(x)$ traces out the Newtonian periodic orbit P_1. Quantum mechanically, however, the particle has a finite probability $|r|^2$ of being reflected at the potential step with reflection amplitude

$$r = \frac{\sqrt{E} - \sqrt{E - V_0}}{\sqrt{E} + \sqrt{E - V_0}}. \tag{2}$$

Note that $\hbar$, Planck's constant, does not appear in Eq. (2) with the consequence that r stays finite in the semiclassical limit $\hbar \to 0$ and even in the classical limit $\hbar = 0$. This observation is the starting point of the theory of ray splitting [8–11] and necessitates the introduction and use of a new nondeterministic, non-Newtonian classical mechanics. More information on the emergence of this new type of mechanics can be found in Ref. [15].

Finiteness of r for $\hbar = 0$ gives rise to the two above-barrier, non-Newtonian, classical orbits P_2 and P_3. Both numerical [9,10] and experimental [14] studies have already confirmed the importance of these two orbits.

For energy E below the barrier V_0, Newtonian mechanics predicts the existence of only the single periodic orbit, P_4.

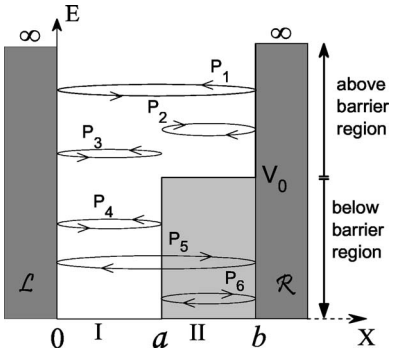

FIG. 1. Types of classical periodic orbits contributing to the quantum dynamics of a particle in the step-in-the-box potential $V_s(x)$. P_1: Newtonian orbit bouncing between the infinite-potential walls $\mathcal{L}$ and $\mathcal{R}$; P_2, P_3: non-Newtonian above-barrier reflection orbits; P_4: Newtonian orbit for $E < V_0$, bouncing between infinite-potential wall $\mathcal{L}$ and the potential step at $x = a$; P_5: ghost orbit with complex action bouncing between infinite-potential walls $\mathcal{L}$ and $\mathcal{R}$; P_6: specter with imaginary action bouncing entirely below the potential barrier V_0.

However, we will show in this paper that to obtain exact periodic-orbit expansions of quantal energy levels in the below-barrier, tunneling regime $E<V_0$, the orbits P_5 and P_6 are equally important. In Newtonian mechanics, these two orbits do not exist. Though Newtonian mechanics is an internally consistent theory, by itself it is insufficient for building exact periodic-orbit expansions. Since part (in the case of P_5) or all (in the case of P_6) of the orbit travels under the potential barrier, these two orbits have complex (P_5) or imaginary (P_6) classical actions. Periodic orbits with complex actions are known to be important in atomic physics [16–18]; they are called ghost orbits in Ref. [19]. Since P_6 has imaginary classical action, we call it a "specter."

Both Newtonian and non-Newtonian ray-splitting orbits were used in Refs. [20–23] to compute exact periodic-orbit expansions of individual energy eigenvalues. This is a new direction in quantum chaos since "traditional" periodic-orbit expansions [2,3,24] provide the level density $\rho(E)$, or the spectral staircase function $N(E)=\int^E \rho(E')dE'$, not individual energy levels E_n. One might argue that since $\rho(E)$ is given by

$$\rho(E)=\sum_{\nu=1}^{\infty}\delta(E-E_\nu), \tag{3}$$

the information about any energy level E_n must be contained in $\rho(E)$. However, if the task is, for instance, to compute E_n for $n=10^6$, this can only be done via $\rho(E)$ by (i) plotting $\rho(E)$ and counting the number of peaks in $\rho(E)$ until one identifies the 10^6th peak and reads off its energy value or (ii) by solving the implicit equation $\min_E\{10^6=N(E)\}$. Generically, this implicit equation is transcendental and its solution requires numerical methods. Moreover, before applying a numerical equation solver, one must run a search algorithm to determine an energy interval in which E_n for $n=10^6$ is located. The crucial advance in Refs. [20,21] is the n-targeted computation of E_n, side-stepping preknowledge of $E_\nu, \nu=1,2,\ldots,n-1$, as well as all counting schemes, and numerical equation solvers, by providing the nth energy level directly (targeted) by the formula

$$E_n=f(n), \tag{4}$$

where f is a known function that can be expressed via a periodic-orbit expansion [20,21]. Thus Eq. (4) is new: a direct periodic-orbit expansion of E_n.

The purpose of our paper is twofold: (i) in Sec. IV, we show that inclusion of ghost orbits yields exact formulas akin to Eq. (4) in the tunneling regime; (ii) in Sec. V, we show how to extract ghost orbit information from computed or measured spectra in the tunneling regime. We call this procedure ghost orbit spectroscopy. Since, in general, the amplitudes of ghost orbits increase as the particle energy $E<V_0$ approaches the threshold $E=V_0$, we focus here on the energy-scaling case

$$V_0=vE. \tag{5}$$

This potential, which Sec. VI shows can be implemented experimentally, allows us to stay close to, but below, the threshold energy V_0 for all E. Equation (5) uses scaled spectroscopy to our advantage in connection with ghost orbit spectroscopy. Note that scaled spectroscopy is already an established experimental technique in atomic physics [16,18,25] and microwave studies [12–14,26].

We organize this paper as follows. To enhance accessibility and readability, Sec. II provides a brief introduction and illustrates, with a simple model system, that periodic-orbit theory is not necessarily an approximate theory. As pointed out above, for many physical and mathematical systems, periodic-orbit theory is exact; the step-in-the-box potential (1), discussed in this paper, provides yet another example. In fact, Ref. [26] conjectures that an exact periodic-orbit theory exists for any bounded quantum system. Section II also introduces basic ideas and notation that will be used throughout this paper. Using the above-barrier case ($E>V_0$) of the step-in-the-box potential (1) as an illustrative example, Sec. III introduces symbolic dynamics [3,27] and a step-function technique for the explicit computation of energy levels. Since the above-barrier case is already well covered in the literature [20–22], Sec. III presents only material essential for the cohesion of this paper. Section IV extends our methods into the tunneling regime ($E<V_0$), where ghost orbits [16–19,22,23] arise. We impose unitarity [23] to obtain exact, convergent ghost orbit expansions of individual energy eigenvalues that the nonunitary theory of Ref. [22] does not achieve [28]. Going far beyond a first announcement of our results in Ref. [23], our periodic-orbit expansions presented here are integral-free. In addition, we discuss their convergence properties in detail. Section V considers the inverse problem of extracting ghost orbit information from a given set of energy levels. We show that a relatively modest number of levels is sufficient (i) to demonstrate the importance of ghost orbits, i.e., their signatures in the Fourier transform of the level density, and (ii) to extract their main physical characteristic, i.e., their complex actions. Section VI proposes an experimental setup that will allow laboratory studies of ghost orbit spectroscopy. This setup also demonstrates that our one-dimensional system is more than an academic example; it has real applications. Section VII discusses our results and compares our unitary, convergent ghost orbit expansions with the nonunitary, divergent theory proposed in Ref. [22]. Section VIII summarizes and concludes the paper.

II. INTRODUCTION TO PERIODIC-ORBIT THEORY

This is a brief introduction to periodic-orbit theory for readers unfamiliar with the topic. Using the infinite square-well potential [29,30] as the example, we illustrate the concepts of Newtonian periodic orbits and their classical actions, and we show how the orbits emerge naturally in the density of states. That periodic-orbit expansions for the infinite square well are exact provides us with an example to illustrate the new concept of direct, exact periodic-orbit expansions of energy levels.

Consider the classical and quantum mechanics of a particle of mass m confined inside the infinite square-well potential of width $2a$ (Fig. 2) given by

$$V_\infty(x)=\begin{cases}0, & \text{for } |x|<a,\\ \infty, & \text{for } |x|\geqslant a.\end{cases} \tag{6}$$

The classical particle bounces periodically between the left-hand wall at $x=-a$ and the right-hand wall at $x=a$. Because

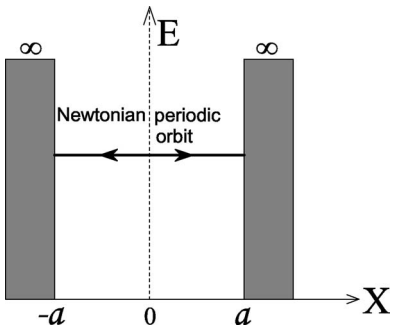

FIG. 2. Newtonian periodic orbit in a square-well potential of width $2a$ and infinitely high walls.

one round trip takes it from $x=-a$ to $x=a$ and back to $x=-a$ along the motion predicted by Newtonian mechanics, we call the corresponding trajectory a Newtonian periodic orbit. The classical action accumulated during one round trip is

$$S(E) = \oint p dx = 4a\sqrt{2mE}, \tag{7}$$

where p is the momentum of the particle.

The Schrödinger equation for a quantal particle of mass m moving nonrelativistically in $V_\infty(x)$ is

$$-\frac{\hbar^2}{2m}\psi''(x) + V_\infty(x)\psi(x) = E\psi(x), \tag{8}$$

where $\hbar$ is Planck's constant. The infinitely steep walls enforce the boundary conditions

$$\psi(\pm a) = 0. \tag{9}$$

Because of the reflection symmetry of $V_\infty(x)$ with respect to $x=0$, $V_\infty(-x)=V_\infty(x)$, Eq. (8) admits two classes of solutions: even states, $\psi^{(+)}(x)$, and odd states, $\psi^{(-)}(x)$. They satisfy

$$\psi^{(\pm)}(-x) = \pm\psi^{(\pm)}(x). \tag{10}$$

The indices "±" in Eq. (10) carry the parity of the wave functions: "+" for positive parity (even states) and "–" for negative parity (odd states). Within $V_\infty(x)$, i.e., for $|x|<a$, the solutions $\psi^{(\pm)}(x)$ of Eq. (8) are oscillatory. Inserting the ansatz

$$\psi^{(-)}(x) = \sin(kx), \tag{11}$$

with k a constant into Eq. (8) yields

$$k = \frac{\sqrt{2mE}}{\hbar}. \tag{12}$$

We suppress the negative k solution since it yields the same wave function (up to a sign) and the same energy levels. Therefore, it is enough to consider $k>0$.

The boundary conditions (9) demand

$$\sin(ka) = 0. \tag{13}$$

Equation (13) is known as a spectral equation. As will become apparent in Secs. III and IV, spectral equations such as Eq. (13) are key to our theory of explicit, periodic-orbit expansions of individual energy eigenvalues. The solutions

$$k_n^{(-)} = \frac{n\pi}{a}, \quad n = 1,2,\ldots \tag{14}$$

determine the negative-parity spectrum of $V_\infty(x)$ according to

$$E_n^{(-)} = \frac{\hbar^2\pi^2 n^2}{2ma^2}. \tag{15}$$

Following similar lines for the positive-parity states, we obtain the spectral equation

$$\cos(ka) = 0 \tag{16}$$

with solutions

$$k_n^{(+)} = \left(n - \frac{1}{2}\right)\frac{\pi}{a}, \quad n = 1,2,\ldots, \tag{17}$$

and the positive-parity energy spectrum

$$E_n^{(+)} = \frac{\hbar^2\pi^2}{2ma^2}\left(n - \frac{1}{2}\right)^2, \quad n = 1,2,\ldots. \tag{18}$$

Now knowing $E_n^{(\pm)}$ explicitly, we may compute the density of states $\rho(E)$ in $V_\infty(x)$. In practice, of course, it is rare to have complete knowledge of the spectrum of a given potential in the form of simple analytical expressions such as Eqs. (15) and (18). Therefore, computing $\rho(E)$ on the basis of a known spectrum seems backward, since in practice it is usually $\rho(E)$ that is either known or can be computed (approximately) using various techniques, and it is the spectrum we seek to compute once we have $\rho(E)$. But much can be learned by first constructing $\rho(E)$ on the basis of a known spectrum, and then, in a second step, recovering this spectrum on the basis of a known $\rho(E)$. It also demonstrates via a simple example that our methods are exact.

The density of states of the positive-parity spectrum

$$\rho^{(+)}(E) = \sum_{n=1}^{\infty} \delta(E - E_n^{(+)}) \tag{19}$$

can be brought via Eq. (18) into the form

$$\rho^{(+)}(E) = \frac{ma}{\hbar^2\pi k}\sum_{n=-\infty}^{+\infty} \delta\left(\frac{ka}{\pi} + \frac{1}{2} - n\right), \tag{20}$$

where $k>0$ is defined in Eq. (12). With the help of the one-periodic δ function,

$$\delta_1(x) = \sum_{n=-\infty}^{+\infty} \delta(x-n) = \sum_{\nu=-\infty}^{+\infty} e^{2\pi i\nu x}, \tag{21}$$

we obtain

$$\rho^{(+)}(E) = \sum_{\nu=-\infty}^{+\infty} (-1)^\nu \frac{2ma^2}{\hbar\pi S(E)} e^{i\nu S(E)/\hbar}. \tag{22}$$

The density of states (22) can be broken up into two parts corresponding to $\nu=0$ and $\nu\neq 0$

$$\rho^{(+)}(E) = \bar{\rho}^{(+)}(E) + \tilde{\rho}^{(+)}(E), \tag{23}$$

where

$$\bar{\rho}^{(+)}(E) = \frac{2ma^2}{\hbar\pi S(E)} = \frac{a\sqrt{m}}{\hbar\pi\sqrt{2E}} \tag{24}$$

corresponds to $\nu=0$, and is called the average density of states, and

$$\tilde{\rho}^{(+)}(E) = \sum_{\nu=1}^{\infty} (-1)^{\nu} \frac{a\sqrt{2m}}{\hbar\pi\sqrt{E}} \cos(2a\nu\sqrt{2mE}/\hbar) \tag{25}$$

corresponds to $\nu \neq 0$, and is called the fluctuating part of the density of states.

Formula (22) illustrates the essence of periodic orbit theory: The density of states, here $\rho^{(+)}(E)$, is expressed in a form that contains only classical quantities [here m and $S(E)$], geometric input (here the width $2a$ of the potential), and Planck's quantum of action $\hbar$. In particular, as shown in Eq. (22), the density of states is expressed as a sum over the product of an amplitude factor $[(-1)^{\nu}2ma^2/\hbar\pi S(E)]$ and a phase factor $e^{i\nu S(E)/\hbar}$ containing multiples ν of the classical action $S(E)$. The index ν is known as the repetition factor, since multiplied by $S(E)$, it corresponds to the total classical action accumulated on multiple traversals of the primitive periodic orbit with action $S(E)$. This orbit is called primitive because it is the shortest one; it cannot be broken down any further into repetitions of a shorter periodic orbit. We mention that in more general cases with smooth potentials, an additional term appears in the periodic-orbit expansion, the so-called Maslov phase [3]. It is a reflection of yet another, important classical property of the periodic orbits: their topology.

Our example has only one primitive periodic orbit, the Newtonian orbit sketched in Fig. 2. More general potentials, such as the step-in-the-box potential $V_s(x)$ shown in Fig. 1, have many, and topologically different, primitive periodic orbits. The orbits $P_1, \ldots, P_6$ in Fig. 1 are examples of primitive periodic orbits for $V_s(x)$; Sec. III shows that many more exist for $V_s(x)$. In these cases, the density of states contains an additional sum over all primitive periodic orbits (see Secs. III and IV).

We now approach our main goal, i.e., the computation of individual energy levels given the density of states

$$\rho(E) = \sum_{\mu=1}^{\infty} \delta(E - E_{\mu}). \tag{26}$$

Suppose examination of a spectral equation, e.g., Eq. (13) or Eq. (16), of a potential reveals an interval $[E_n^{(1)}, E_n^{(2)}]$ in which only the single energy level E_n is found. Since the end points $E_n^{(1)}$ and $E_n^{(2)}$ delimit an interval in which E_n, a root of the spectral equation, can be found, we call $[E_n^{(1)}, E_n^{(2)}]$ the root interval of E_n, and since $E_n^{(1)}$ and $E_n^{(2)}$ separate (isolate) the spectral point E_n from all the other roots of the spectral equation, we call $E_n^{(1)}$ and $E_n^{(2)}$ root separators. Of course, for a general bounded system without degeneracies, the root separators are not unique. This introduces a welcome flexibility into the theory.

Integrating over the root interval $[E_n^{(1)}, E_n^{(2)}]$, we have

$$E_n = \int_{E_n^{(1)}}^{E_n^{(2)}} E\rho(E)dE, \tag{27}$$

since according to the definition of $E_n^{(1)}$ and $E_n^{(2)}$ only the δ function $\delta(E-E_n)$ of the sum over δ functions in Eq. (26) contributes and "projects" E onto E_n in Eq. (27).

Equation (27) is the starting point for obtaining periodic-orbit expansions of individual energy eigenvalues. We illustrate the technique with the help of the positive-parity spectrum of $V_{\infty}(x)$. Suitable root separators for $E_n^{(+)}$ are $E_n^{(1)} = \hbar^2(n-1)^2\pi^2/2ma^2$ and $E_n^{(2)} = \hbar^2 n^2\pi^2/2ma^2$. We then have

$$E_n^{(+)} = \int_{E_n^{(1)}}^{E_n^{(2)}} E\rho^{(+)}(E)dE. \tag{28}$$

Using the periodic-orbit expansion (22) of $\rho^{(+)}(E)$, we obtain

$$E_n^{(+)} = F(E_n^{(2)}) - F(E_n^{(1)}), \tag{29}$$

where $F(E)$ is the indefinite integral

$$F(E) = \int E\rho^{(+)}(E)dE, \tag{30}$$

given explicitly by

$$F(E) = \frac{[S(E)]^3}{48\hbar\pi ma^2} + \frac{\hbar^2}{8m\pi a^2}\sum_{\nu=1}^{\infty}(-1)^{\nu}\left\{\frac{1}{\nu}\left[\left(\frac{S(E)}{\hbar}\right)^2 - \frac{2}{\nu^2}\right]\sin\left(\frac{\nu S(E)}{\hbar}\right) + \frac{2}{\nu^2}\frac{S(E)}{\hbar}\cos\left(\frac{\nu S(E)}{\hbar}\right)\right\} \tag{31}$$

with $S(E)$, the action of the Newtonian periodic orbit, defined in Eq. (7). Using Eq. (31) in Eq. (29), we obtain a periodic-orbit expansion for the individual energy levels $E_n^{(+)}$. With Eq. (7), Eq. (31), and formula 0.2341 of Ref. [31], viz.,

$$\sum_{\nu=1}^{\infty}(-1)^{\nu+1}\frac{1}{\nu^2} = \frac{\pi^2}{12}, \tag{32}$$

Eq. (29) can be evaluated explicitly to yield Eq. (18). This means that Eq. (29) reproduces the correct result for $E_n^{(+)}$.

At this point, we have come full circle. Starting from Eq. (18) we computed $\rho^{(+)}(E)$, Eq. (22), and then used $\rho^{(+)}(E)$ to compute $E_n^{(+)}$ [Eq. (18)] directly in the form of a periodic-orbit expansion [Eq. (29)] via the "projector equation" (27).

Our main result is Eq. (29), the periodic-orbit expansion of all individual energy levels of the positive-parity spectrum of $V_{\infty}(x)$ in the form $E_n^{(+)} = f^{(+)}(n)$, where the structure of $f^{(+)}$ is fixed and known. Thus, computation of $E_n^{(+)}$ requires nothing more than "plugging" n into the argument of $f^{(+)}$. Similar calculations can be performed for the negative-parity case to yield an explicit periodic-orbit expansion of the negative-parity energy levels $E_n^{(-)} = f^{(-)}(n)$ analogous to Eq. (29).

In summary, we have shown how knowledge of the level density combined with root separators can be used to obtain exact periodic-orbit expansions of individual energy levels.

Illustrating the method with an elementary textbook example, the infinite square-well potential $V_\infty(x)$, we see how the method works generally as soon as $\rho(E)$ and the root separators are known.

III. SCALING STEP-IN-THE-BOX POTENTIAL: BRIEF REVIEW OF THE ABOVE-BARRIER CASE

In Sec. II, we showed how a periodic-orbit theory based on Newtonian periodic orbits yields exact periodic-orbit expansions of the density of states and individual energy eigenvalues of a model potential. In general, however, Newtonian periodic orbits alone do not allow us to obtain exact periodic-orbit expansions of the density of states $\rho(E)$ or individual energy levels E_n. Orbits not allowed by Newtonian mechanics must be included in the periodic-orbit expansions. This section focuses on the case $E>V_0$ of the step-in-the-box potential (see Fig. 1) and shows how the non-Newtonian periodic orbits P_2 and P_3 in Fig. 1 emerge naturally as essential ingredients for exact periodic-orbit expansions. To prepare for the scaling, below-barrier case treated in Secs. IV and V, we focus first on the scaling above-barrier case $V_0=vE$ with $v<1$ $(E>V_0)$ and use it to present a method for obtaining periodic-orbit expansions which is based directly on the spectral equation and yields periodic-orbit expansions via a staircase function with unit step and a distance between steps of 2π.

Section II motivated the need for summing over all primitive periodic orbits in a periodic-orbit expansion of $\rho(E)$, or the energy levels E_n themselves. Since it turns out that $V_s(x)$ contains an infinite number of primitive periodic orbits, we require a scheme to label and enumerate them all. Symbolic dynamics [3,27] provides this scheme.

For $V_s(x)$, a simple binary code suffices [32], which we construct in the following way. First, as shown in Fig. 1, we label the left-hand and right-hand walls of $V_s(x)$ with the symbols $\mathcal{L}$ and $\mathcal{R}$, respectively. Any trajectory in $V_s(x)$, not necessarily periodic, can now be labeled with the two symbols $\mathcal{L}$ and $\mathcal{R}$ if the motion is restricted to the four possible "events": (i) reflection off $\mathcal{L}$; (ii) reflection off $\mathcal{R}$; (iii) reflection off the potential step at $x=a$; (iv) transmission through the potential step, and free motion between events otherwise. Any finite history of events can be mapped onto "words" w of finite lengths over the two binary symbols $\mathcal{L}$ and $\mathcal{R}$. The word $\mathcal{LRL}$, e.g., denotes a trajectory which bounces off $\mathcal{L}$, transmits through the step, bounces off $\mathcal{R}$, transmits a second time through the step, bounces off $\mathcal{L}$, proceeds to bounce off the step, and finally returns to its starting point. Apparently, we can form 2^N words w of length N with the two symbols $\mathcal{L}$ and $\mathcal{R}$. While trajectories represented by the words w still have their history encoded in the sequence of symbols of w, in particular what event is the starting event of the trajectory and what event terminates it, this level of detail is not necessary for periodic orbits. Periodic orbits are coded with the help of cyclic symbol strings $\tilde{w}$, which can be imagined as words w arranged in a circle. Obviously, many words w become identical when turned into cyclic symbol strings $\tilde{w}$. Examples are $w_1=\mathcal{LRL}$ and $w_2=\mathcal{RLL}$. Obviously $\tilde{w}_1=\tilde{w}_2$. Because we imagine the symbols arranged in a circle like pearls on a string, we call the set of mutually different cyclic symbol strings necklaces [33] and denote them by $\hat{w}$. For example, if $\tilde{w}_1=\mathcal{LRL}$, $\tilde{w}_2=\mathcal{RLL}$, and $\tilde{w}_3=\mathcal{RRL}$, then $\tilde{w}_1=\tilde{w}_2\neq\tilde{w}_3$. In general, two necklaces $\tilde{w}_1$ and $\tilde{w}_2$ are equal if there exists a rotation of the symbols of $\tilde{w}_2$ such that $\tilde{w}_1$ and $\tilde{w}_2$ are congruent.

We may now code all periodic orbits shown in Fig. 1 with the $\mathcal{L}$, $\mathcal{R}$ scheme. The Newtonian periodic orbit is coded $\mathcal{LR}$; the non-Newtonian orbits P_2 and P_3 are coded $\mathcal{R}$ and $\mathcal{L}$, respectively; the Newtonian orbit P_4 is coded $\mathcal{L}$; and the ghost orbits P_5 and P_6 are coded $\mathcal{LR}$ and $\mathcal{R}$, respectively.

At a fixed energy E, the coding scheme is unique. Each necklace $\hat{w}$ corresponds one-to-one to a periodic orbit. At different energies, however, qualitatively different orbits (such as P_3 and P_4, for example) may correspond to the same necklace $\hat{w}$ ($\hat{w}=\mathcal{L}$ in our example). In periodic-orbit theory this is never a problem, since $\rho(E)$, e.g., is evaluated at a given value of E, for which the naming scheme is unique.

It is possible and useful to define functions $f(w)$ over the set of words $\{w\}$ and functions $\hat{f}(\hat{w})$ over the set $\{\hat{w}\}$ of necklaces. Excellent examples are the six counting functions $n_{\mathcal{L}}(w)$, $n_{\mathcal{R}}(w)$, $n_{\mathcal{LL}}(w)$, $n_{\mathcal{RR}}(w)$, $n_{\mathcal{LR}}(w)$, $n_{\mathcal{RL}}(w)$ that count the number of $\mathcal{L}$ symbols, $\mathcal{R}$ symbols, $\mathcal{LL}$ pairs, $\mathcal{RR}$ pairs, $\mathcal{LR}$ combinations, and $\mathcal{RL}$ combinations, respectively. In the case of $n_{\mathcal{L}}$ and $n_{\mathcal{R}}$, it makes no difference whether they are applied to words w or necklaces $\hat{w}$; we have $n_{\mathcal{L}}(w)=\hat{n}_{\mathcal{L}}(\hat{w})$ and $n_{\mathcal{R}}(w)=\hat{n}_{\mathcal{R}}(\hat{w})$. In the case of the other four counting functions, however, it usually makes a difference whether they are applied to a word w or a necklace $\hat{w}$. We have, e.g., $n_{\mathcal{LL}}(\mathcal{LRL})=0$, but $\hat{n}_{\mathcal{LL}}(\mathcal{LRL})=1$; $n_{\mathcal{RR}}(\mathcal{RRR})=2$, but $\hat{n}_{\mathcal{RR}}(\mathcal{RRR})=3$; $n_{\mathcal{LR}}(\mathcal{RL})=0$, but $\hat{n}_{\mathcal{LR}}(\mathcal{RL})=1$; $n_{\mathcal{RL}}(\mathcal{LR})=0$, but $\hat{n}_{\mathcal{RL}}(\mathcal{LR})=1$. Note, in particular, that $n_{\mathcal{RL}}(\mathcal{R})=0$, but $\hat{n}_{\mathcal{RR}}(\mathcal{R})=1$; $n_{\mathcal{LL}}(\mathcal{L})=0$, but $\hat{n}_{\mathcal{LL}}(\mathcal{L})=1$.

With the help of the counting functions, we define four functions that turn out to be useful later

$$l(w)=n_{\mathcal{L}}(w)+n_{\mathcal{R}}(w),$$

$$\alpha(w)=n_{\mathcal{LL}}(w)+n_{\mathcal{RR}}(w),$$

$$\beta(w)=n_{\mathcal{LR}}(w)+n_{\mathcal{RL}}(w),$$

$$\chi(w)=l(w)+n_{\mathcal{RR}}(w). \tag{33}$$

Their necklace versions $\hat{l}(\hat{w})$, $\hat{\alpha}(\hat{w})$, $\hat{\beta}(\hat{w})$, and $\hat{\chi}(\hat{w})$ are constructed analogously as explained above.

We now turn to the nonrelativistic quantum mechanics of $V_s(x)$. In $[0,a]$, the wave function of a quantum particle of mass m moving in $V_s(x)$ is given by $\psi(x)=\sin(kx)$; in $[a,b]$ it is $\psi(x)=A\sin[\kappa(x-b)]$, where A is a constant, $k=\sqrt{2mE/\hbar}$, and $\kappa=\sqrt{2m(E-V_0)}/\hbar=\eta k$ with $\eta=\sqrt{1-v}$. Continuity of $\psi(x)$ and its first derivative at $x=a$ yield the spectral equation

$$\sin(ka+\kappa d)=r\sin(ka-\kappa d), \tag{34}$$

where $r=(1-\eta)/(1+\eta)$ and $d=b-a$. Defining

$$\gamma=\frac{\eta d}{a}, \tag{35}$$

$$\omega = \frac{1-\gamma}{1+\gamma}, \tag{36}$$

and

$$\xi = ka(1+\gamma), \tag{37}$$

we obtain the dimensionless spectral equation

$$\sin(\xi) = r\sin(\omega\xi), \tag{38}$$

where $0<r<1$ and $0<\omega<1$. It is straightforward to prove that (38) has only real solutions ξ_n. We arrange the index n in such a way that $\xi_0=0$, and ξ_1 is the first positive root of Eq. (38). We have $\xi_{-n}=-\xi_n$. Because $r<1$, one and only one root of Eq. (38) (namely ξ_n) occurs in the root interval

$$I_n = \left[\left(n-\frac{1}{2}\right)\pi, \left(n+\frac{1}{2}\right)\pi\right]. \tag{39}$$

Thus all roots of Eq. (38) have multiplicity 1 and $\xi_n^{(1)}=(n-1/2)\pi$, $\xi_n^{(2)}=(n+1/2)\pi$ are the root separators of ξ_n.

Consider the matrix

$$S(\xi) = \begin{pmatrix} 0 & re^{iu_+\xi} & te^{iu_+\xi} & 0 \\ -e^{iu_+\xi} & 0 & 0 & 0 \\ 0 & 0 & 0 & -e^{iu_-\xi} \\ 0 & te^{iu_-\xi} & -re^{iu_-\xi} & 0 \end{pmatrix}, \tag{40}$$

where $t=\sqrt{1-r^2}$, and

$$u_+ = \frac{(1+\omega)}{2}, \quad u_- = \frac{(1-\omega)}{2}. \tag{41}$$

We have

$$\det(S-1) = -2ie^{i\xi}[\sin(\xi) - r\sin(\omega\xi)]. \tag{42}$$

Therefore, the equation $\det(S-1)=0$ and Eq. (38) have the same roots. Because the matrix S defined in Eq. (40) is unitary, we may write it as

$$S(\xi) = U(\xi)\mathrm{diag}(e^{i\phi_1(\xi)}, \ldots, e^{i\phi_4(\xi)})U(\xi)^\dagger, \tag{43}$$

where $U(\xi)$ is unitary and $\phi_j(\xi)$, $j=1,\ldots,4$ are real functions of ξ (eigenphases of S). Therefore, we encounter a root of $\det(S-1)=0$, or equivalently, a root of Eq. (38), whenever any of the phases $\phi_1(\xi),\ldots,\phi_4(\xi)$ is an integer multiple of 2π.

It is straightforward to compute the phases analytically. They are given by

$$\phi_1(\xi) = \frac{1}{2}\{\xi - \arcsin[r\sin(\omega\xi)]\}, \quad \phi_2(\xi) = \phi_1(\xi) + \pi, \tag{44}$$

$$\phi_3(\xi) = \frac{1}{2}\{\xi + \arcsin[r\sin(\omega\xi)] + \pi\}, \quad \phi_4(\xi) = \phi_3(\xi) + \pi; \tag{45}$$

all four are monotonically increasing functions of ξ.

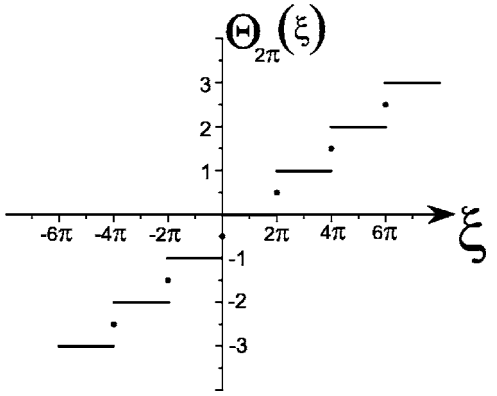

FIG. 3. Staircase function $\Theta_{2\pi}(\xi)$. This function jumps by one unit whenever its argument ξ crosses a multiple of 2π.

We now define the counting function

$$\mathcal{N}(\xi) = \sum_{n=1}^{\infty} \theta(\xi - \xi_n) \tag{46}$$

of the positive zeros of Eq. (38), where

$$\theta(\xi) = \begin{cases} 0, & \text{for } \xi<0, \\ 1/2, & \text{for } \xi=0, \\ 1, & \text{for } \xi>0 \end{cases} \tag{47}$$

is Heaviside's step function. Define the function (see Fig. 3)

$$\Theta_{2\pi}(\xi) = -\frac{1}{2} + \frac{\xi}{2\pi} + \frac{1}{\pi}\sum_{n=1}^{\infty}\frac{\sin(n\xi)}{n} = \begin{cases} m-\frac{1}{2}, & \text{for } \xi = 2\pi m, \\ m, & \text{for } 2\pi m < \xi < 2\pi(m+1), \end{cases} \tag{48}$$

where m is an integer. This function is a "staircase function." It jumps by one unit whenever ξ crosses a multiple of 2π.

With the help of $\Theta_{2\pi}$, and because all roots of Eq. (38) have multiplicity 1 (see above), we can now relate $\mathcal{N}(\xi)$ to the eigenphases of $S(\xi)$

$$\mathcal{N}(\xi) = \sum_{j=1}^{4}\Theta_{2\pi}[\phi_j(\xi)] = -\frac{1}{2} + \frac{\xi}{\pi} + \frac{1}{\pi}\sum_{k=1}^{4}\sum_{n=1}^{\infty}\frac{\sin[n\phi_k(\xi)]}{n}. \tag{49}$$

Because of the unitarity of $S(\xi)$, and using the symbols Im and Tr to denote the imaginary part and the trace of a matrix, respectively, we write Eq. (49) in the form

$$\mathcal{N}(\xi) = -\frac{1}{2} + \frac{\xi}{\pi} + \frac{1}{\pi}\,\mathrm{Im}\,\mathrm{Tr}\sum_{n=1}^{\infty}\frac{1}{n}S^n(\xi). \tag{50}$$

We obtain the density of states $\rho(\xi)$ from the staircase function $\mathcal{N}(\xi)$ via

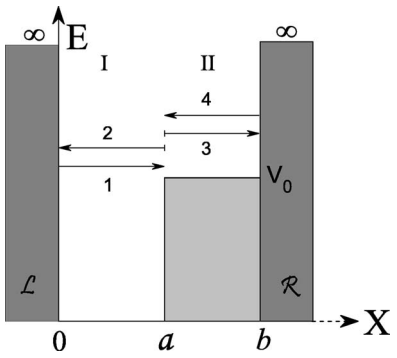

FIG. 4. Channel assignments inside the step-in-the-box potential $V_s(x)$.

$$\rho(\xi) = \frac{d\mathcal{N}(\xi)}{d\xi}. \tag{51}$$

Since $\rho(\xi)$ is now known, we obtain ξ_n in analogy to Eq. (27) according to [20–22]

$$\xi_n = \int_{(n-1/2)\pi}^{(n+1/2)\pi} \xi\rho(\xi)d\xi = \left[\xi\mathcal{N}(\xi)\right]_{(n-1/2)\pi}^{(n+1/2)\pi} - \int_{(n-1/2)\pi}^{(n+1/2)\pi} \mathcal{N}(\xi)d\xi$$
$$= \left(2n - \frac{1}{2}\right)\pi - \int_{(n-1/2)\pi}^{(n+1/2)\pi} \mathcal{N}(\xi)d\xi, \tag{52}$$

where we used $\mathcal{N}[(n+1/2)\pi]=n$ and $\mathcal{N}[(n-1/2)\pi]=n-1$. This is an explicit expression for ξ_n, since the right-hand side of (52) involves only known functions of ξ. With Eq. (50), exchanging integration and summation (which is allowed here [21]), and using the fact that the trace of odd powers of S is zero, we obtain

$$\xi_n = n\pi - \frac{1}{2\pi}\,\mathrm{Im\,Tr}\sum_{m=1}^{\infty}\frac{1}{m}\int_{(n-1/2)\pi}^{(n+1/2)\pi} S^{2m}(r,\omega;\xi)d\xi. \tag{53}$$

An integral-free representation of ξ_n is obtained by relating the trace of the powers of the S matrix in Eq. (53) to the periodic orbits, Newtonian and non-Newtonian, in the potential $V_s(x)$ (see Fig. 1). This is accomplished by realizing that the matrix S defined in Eq. (40) has a physical interpretation as the scattering matrix of $V_s(x)$. We see this in the following way. Define four channels of $V_s(x)$ represented by the four arrows in Fig. 4. Channel number 1 (arrow number 1) corresponds to a particle moving from $x=0$ to $x=a$; channel number 2 (arrow number 2) corresponds to a particle moving in the opposite direction, from $x=a$ to $x=0$. Channel number 3 corresponds to a particle moving from $x=a$ to $x=b$ (arrow number 3), and channel number 4 corresponds to a particle moving in the opposite direction from $x=b$ to $x=a$ (arrow number 4). The connection between the classical paths and the powers of the S matrix in Eq. (53) is achieved by realizing that the channels (arrows) can be interpreted both classically, as sections of particle trajectories, and quantum mechanically, as quantum flux streaming along the channels in the direction indicated by the arrows. The matrix element S_{12}, e.g., corresponds to a particle, classical or quantum mechanical, traversing channel number 1 in the direction of arrow number 1 and, having reflected at the step at $x=a$, just about to enter channel number 2 at $x=a$. Therefore, quantum mechanically, we can construct the amplitude in this channel by $S_{12}=re^{iu_+\xi}$, where r is the reflection amplitude and $u_+\xi$ is the action accumulated by traversing channel 1 on its way to channel 2. All the other matrix elements of S in Eq. (40) have a similar physical interpretation. The nth power of S, S^n, corresponds to a particle moving inside $V_s(x)$ on a path consisting of the four sections (arrows) in Fig. 4 as building blocks. Let us examine, e.g., the matrix element $(S^2)_{11}$ given by

$$(S^2)_{11} = \sum_{j=1}^{4} S_{1j}S_{j1}. \tag{54}$$

The sum in Eq. (54) consists of four terms, $S_{11}S_{11}$, $S_{12}S_{21}$, $S_{13}S_{31}$, and $S_{14}S_{41}$. According to Eq. (40), S_{11} is zero, because the tip of the arrow number 1 cannot be continuously connected to its tail; in other words, flux cannot feed continuously from the tip of arrow number 1 back to its tail. $S_{12}S_{21}$, however, defines an allowed path since the tip of arrow number 1 joins smoothly with the tail of arrow number 2. The flux then traverses arrow number 1 and returns on arrow number 2, defining a periodic orbit. This way we see by example that all diagonal elements of S^n correspond to periodic orbits, and that the trace of S^n corresponds to a sum of periodic orbits. In fact, by writing out a few powers of S explicitly, we see that

$$\mathrm{Tr}(S^{2m}) = 2\sum_{w,l(w)=m}(-1)^{\hat{\chi}(\hat{w})}r^{\hat{\alpha}(\hat{w})}t^{\hat{\beta}(\hat{w})}e^{2i\sigma(w)\xi}, \tag{55}$$

i.e., the trace of S^{2m} is twice the sum over all 2^m binary words w with fixed length $l(w)=m$. The "hat" symbol $(\hat{})$ turns words into necklaces. The functions $\hat{\chi}(\hat{w})$, $\hat{\alpha}(\hat{w})$, $\hat{\beta}(\hat{w})$, the necklace analogues of the word functions (33), and the function $\sigma(w)$, defined below, have the following physical interpretation.

Each term in Eq. (55) corresponds to an amplitude factor, $(-1)^{\hat{\chi}(\hat{w})}r^{\hat{\alpha}(\hat{w})}t^{\hat{\beta}(\hat{w})}$, which keeps track of reflections and transmissions of a particular orbit coded by w, and a phase factor $e^{2i\sigma(w)\xi}$, which represents the total action accumulated along the orbit w. The function $\hat{\chi}(\hat{w})$ counts how many times the orbit w reflects off the two walls of $V_s(x)$ and how many times it reflects off the step at $x=a$, but only if it approaches the step in channel 4 and gets scattered into channel 3. The function $\hat{\alpha}(\hat{w})$ counts the total number of reflections at $x=a$ (channel 1 to channel 2 plus channel 4 to channel 3) and $\hat{\beta}(\hat{w})$ counts the total number of transmissions through the step at $x=a$ (channel 1 to channel 3 plus channel 4 to channel 2). The action function $\sigma(w)$ is defined as

$$\sigma(w) = n_{\mathcal{L}}(w)u_+ + n_{\mathcal{R}}(w)u_-, \tag{56}$$

where $n_{\mathcal{L}}$ and $n_{\mathcal{R}}$ are the counting functions of $\mathcal{L}$ and $\mathcal{R}$ symbols, respectively, and u_+, u_- are defined in Eq. (41).

Inserting Eq. (55) into Eq. (53) and performing the integration, we obtain

$$\xi_n = n\pi - \frac{1}{\pi}\sum_{m=1}^{\infty}\frac{1}{m}\sum_{w,l(w)=m} P(w)G_n[\sigma(w)], \tag{57}$$

where

$$P(w) = (-1)^{\hat{\chi}(\hat{w})} r^{\hat{\alpha}(\hat{w})} t^{\hat{\beta}(\hat{w})} \tag{58}$$

and

$$G_n(w) = \frac{1}{\sigma(w)}\sin[2\pi n\sigma(w)]\sin[\pi\sigma(w)]. \tag{59}$$

In Eq. (57), we must sum over all words w of length $l(w)=m$. Let us inspect a word w of length m. Such a word can always be written as

$$w = \underbrace{w_p \oplus w_p \oplus \cdots \oplus w_p}_{\nu \text{ times}}, \tag{60}$$

where w_p is the smallest symbol unit contained in w that, when repeated ν times, results in w. The word w_p is also called the "primitive root" of w. Let l_p be the length of w_p, i.e., $l_p = l(w_p)$. Then we have

$$m = \nu l_p. \tag{61}$$

There are l_p words, different from w, but cyclically equivalent to w. We note that both $P(w)$ and $G_n(w)$ are invariant under cyclic permutations of the symbols of w. Therefore, using the necklace $\hat{w}_p$ as the representative of w and its l_p cyclical equivalents, the sum over the words w in Eq. (57) can be written as a sum over the necklaces $\hat{w}_p$, supplemented with proper repetition factors, according to

$$\xi_n = n\pi - \frac{1}{\pi}\sum_{\hat{w}_p}\sum_{\nu=1}^{\infty}\frac{1}{\nu\, l_p} l_p P(\hat{w}_p)^{\nu} G_n[\nu\sigma(\hat{w}_p)]. \tag{62}$$

From Eq. (62) we obtain the final result for the periodic-orbit expansion of ξ_n in the form

$$\xi_n = n\pi - \frac{1}{\pi}\sum_{\hat{w}_p}\sum_{\nu=1}^{\infty}\frac{1}{\nu^2}[(-1)^{\hat{\chi}(\hat{w}_p)} r^{\hat{\alpha}(\hat{w}_p)} t^{\hat{\beta}(\hat{w}_p)}]^{\nu} \times \frac{1}{\sigma(\hat{w}_p)}\sin[\pi\nu\sigma(\hat{w}_p)]\sin[2\pi\nu n\sigma(\hat{w}_p)]. \tag{63}$$

We have achieved our aim of deriving an explicit, exact, integral-free, periodic-orbit expansion of the roots of the spectral equation (38). With ξ_n computed, the above-barrier energy spectrum of $V_s(x)$ is now calculated according to

$$E_n = \frac{\hbar^2}{2m}\frac{\xi_n^2}{[a + d\sqrt{1-v}]^2}. \tag{64}$$

IV. BELOW-BARRIER CASE

We now turn to the below-barrier case $E < V_0$, which corresponds to $v > 1$. Again we match at $x=a$ the wave function $\psi_I(x)=\sin(kx)$, valid in $0 \leq x \leq a$ and the wave function $\psi_{II}(x)=A\sinh[\kappa(x-b)]$, valid in $a \leq x \leq b$, where κ

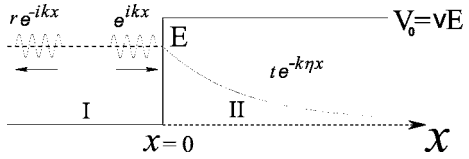

FIG. 5. A plane wave e^{ikx} incident from the left in region I on a step of height $V_0 > E$ is reflected off the step to the left with amplitude r, where $|r|=1$. The wave tunnels into region II, $te^{-k\eta x}$, but is exponentially attenuated.

$= \sqrt{2m(V_0-E)}/\hbar = \eta k$, $\eta = \sqrt{v-1}$, to obtain the spectral equation

$$\tan(ka) = -\frac{1}{\eta}\tanh(k\eta d), \tag{65}$$

with, as in Sec. III, $d=b-a$. The singularity-free version of Eq. (65) is

$$\eta\sin(ka)\cosh(\eta kd) + \cos(ka)\sinh(\eta kd) = 0. \tag{66}$$

We give both versions of the spectral equation since Eq. (65) is better suited for the computation of root separators, while Eq. (66) occurs naturally in connection with the S-matrix theory discussed below.

To derive a periodic-orbit solution for the roots of (65) [(66), respectively], we need the reflection coefficient in the case $d \to \infty$, i.e., the subbarrier reflection coefficient r, for a step potential with infinitely long plateaus. Figure 5 illustrates the situation. In region I ($x<0$) the wave function is $\psi_I(x) = e^{ikx} + re^{-ikx}$; in region II it is $\psi_{II}(x) = te^{-k\eta x}$. Continuity of the wave function and its first derivative at $x=0$ yield

$$r = \frac{1 - i\eta}{1 + i\eta}. \tag{67}$$

We now compute the reflection coefficient R for the case of finite d and express it with the help of r. For finite d, we refer to Fig. 6 and have $\psi_I(x) = e^{ikx} + Re^{-ikx}$, and $\psi_{II}(x) = T\sinh[\eta k(x-d)]$. Imposing continuity of the wave function and its first derivative at $x=0$ gives

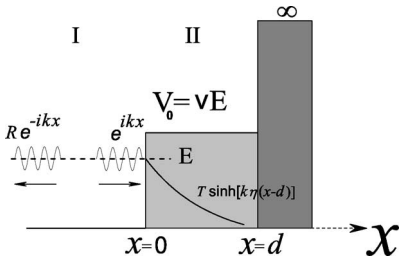

FIG. 6. Similar to Fig. 5, with one crucial difference: The plateau of the step potential, extending to $+\infty$ in Fig. 5, terminates with an infinitely high wall at $x=d$. This changes the reflection and transmission coefficients of the wave from r to R and from t to T, respectively.

$$R(k) = \frac{i\sinh(\eta kd) + \eta\cosh(\eta kd)}{i\sinh(\eta kd) - \eta\cosh(\eta kd)} = r\frac{1 - r^* e^{-2\eta kd}}{1 - re^{-2\eta kd}}. \quad (68)$$

Note that R is a function of k, while r is a constant. Define the dimensionless variable $\xi = ka$ and note that this ξ differs from ξ defined for the above-barrier case in Sec. III [see Eq. (37)]. With γ defined in Eq. (35), we obtain the dimensionless spectral equations

$$\tan(\xi) = -\frac{1}{\eta}\tanh(\gamma\xi), \quad (69)$$

or

$$\eta\sin(\xi)\cosh(\gamma\xi) + \cos(\xi)\sinh(\gamma\xi) = 0, \quad (70)$$

respectively. Equation (68) becomes

$$R(\xi) = \frac{i\tanh(\gamma\xi) + \eta}{i\tanh(\gamma\xi) - \eta} = r\frac{1 - r^* e^{-2\gamma\xi}}{1 - re^{-2\gamma\xi}}. \quad (71)$$

There is another way of deriving the spectral equation in the case $E < V_0$. Lowering E below V_0 turns Eq. (2) into

$$r = \frac{k - i\kappa}{k + i\kappa} = \frac{1 - i\eta}{1 + i\eta}, \quad (72)$$

consistent with Eq. (67). Moreover, for $E < V_0$, the spectral equation (34) turns into

$$\sin(ka + i\kappa d) = r\sin(ka - i\kappa d), \quad (73)$$

which is the same as the spectral equation (66). Here it is important to notice that $i\kappa d$ in Eq. (73) is the complex action of a classical trajectory with $E < V_0$, starting at $x = a$ and ending at $x = b$: The classically forbidden section $a < x < b$ makes an imaginary contribution $i\kappa d$ to the classical action of this trajectory. As discussed in the introduction, classical trajectories with complex actions are known as ghost orbits in the literature [16–19,22,23]. We interpret the action $i\kappa d$ as one half of the action of the specter P_6 in Fig. 1. In the scaled case, γ is the scaled, under-barrier action of a classical trajectory traveling from $x = a$ to $x = b$, or from $x = b$ to $x = a$. We interpret it as one half of the scaled action of the specter P_6 in Fig.1.

In analogy with the above-barrier case discussed in Sec. III, we would like to express the spectral equation (70) in the form $\det(S - 1) = 0$, where S is the below-barrier scattering matrix of $V_s(x)$. Section III showed that for $E > V_0$ there are four open channels, which we called channels 1, 2, 3, and 4, respectively. However, when lowering the energy through $E = V_0$, channels 3 and 4 close at $E = V_0$, leaving only two open channels (channels 1 and 2) in the energy regime $E < V_0$. Thus, for $E < V_0$, the scattering matrix turns into a 2×2 matrix, given by

$$S(\xi) = \begin{pmatrix} 0 & R(\xi)e^{i\xi} \\ -e^{i\xi} & 0 \end{pmatrix}. \quad (74)$$

Direct calculation shows that

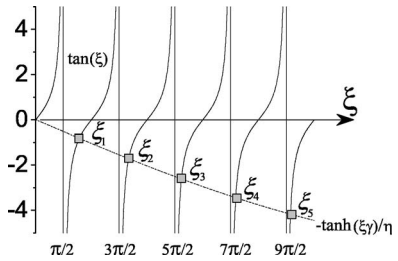

FIG. 7. Graphical solution of the spectral equation (69) illustrating the concept of root separators. According to Eq. (69) the roots of the spectral equation (gray squares) are given by the intersections of the functions $\tan(\xi)$ (solid lines) and $-\tanh(\gamma\xi)/\eta$ (dashed line). Each root ξ_n (gray squares) of the spectral equation (69) is located between its root separators $(n-1/2)\pi$ and $(n+1/2)\pi$, respectively.

$$\det(S - 1) = \frac{2e^{i\xi}}{\sinh(\gamma\xi) + i\eta\cosh(\gamma\xi)}\{\eta\sin(\xi)\cosh(\gamma\xi) + \cos(\xi)\sinh(\gamma\xi)\}. \quad (75)$$

Since the prefactor in Eq. (75) never vanishes, $\det(S-1) = 0$ has the same roots as, and is therefore equivalent to, the spectral equation (70).

We note that

$$S^2(\xi) = -R(\xi)e^{2i\xi}I, \quad (76)$$

where I is the 2×2 unit matrix. Therefore,

$$S^{2m}(\xi) = (-1)^m R^m(\xi)e^{2im\xi}I, \quad m = 1,2,\ldots. \quad (77)$$

We now study the structure of the roots of the spectral equation (69): These roots are given by the intersections of the functions $\tan(\xi)$ and $-\tanh(\gamma\xi)/\eta$ as shown in Fig. 7. According to Fig. 7, the nth root of Eq. (69) lies in the root interval

$$\left(n - \frac{1}{2}\right)\pi < \xi_n < \left(n + \frac{1}{2}\right)\pi. \quad (78)$$

To apply the staircase-function method of Sec. III for the explicit computation of the roots ξ_n, we need the eigenangles $\phi_1(\xi)$ and $\phi_2(\xi)$ of the S matrix (74), which is straightforward because S is only a 2×2 matrix. From $\det[S(\xi) - \Lambda I] = 0$, we obtain

$$\Lambda^2 = -R(\xi)e^{2i\xi}, \quad (79)$$

where $R(\xi)$ is defined in Eq. (71). Defining

$$\varphi(\xi) = \arctan\left[\frac{1}{\eta}\tanh(\gamma\xi)\right], \quad (80)$$

we may write

$$-R(\xi) = e^{2i\varphi(\xi)} \quad (81)$$

and, therefore,

$$\phi_1(\xi) = \xi + \varphi(\xi), \quad \phi_2(\xi) = \xi + \pi + \varphi(\xi). \quad (82)$$

That the two eigenangles $\phi_1(\xi)$ and $\phi_2(\xi)$ are monotonically increasing functions of ξ, together with the equivalence of $\det(S-1) = 0$ and the spectral equation (70), allows us to use

the staircase-function approach of Sec. III to compute the roots ξ_n. With $\Theta_{2\pi}$ defined in Eq. (48), we have

$$\mathcal{N}(\xi) = \sum_{j=1}^{2} \Theta_{2\pi}[\phi_j(\xi)] = -\frac{1}{2} + \frac{\xi}{\pi} + \frac{\varphi(\xi)}{\pi} + \frac{1}{\pi}\sum_{j=1}^{2}\sum_{n=1}^{\infty} \frac{\sin[n\phi_j(\xi)]}{n} = -\frac{1}{2} + \frac{\xi}{\pi} + \frac{\varphi(\xi)}{\pi} + \frac{1}{2\pi}\,\mathrm{Im\,Tr}\sum_{m=1}^{\infty}\frac{1}{m}S^{2m}(\xi), \tag{83}$$

where, just as in Sec. III, we made use of the trace of the odd powers of $S(\xi)$ being zero. Formula (52) remains valid since, according to Eqs. (39) and (78), the above-barrier and the below-barrier cases have the same root separators. We turn it into the analogue of Eq. (53) by carefully noting that according to Eq. (83), the staircase function in the below-barrier case contains an extra phase factor $\varphi(\xi)$. Then, we obtain

$$\xi_n = n\pi - \frac{\Phi_n}{\pi} - \frac{1}{2\pi}\,\mathrm{Im\,Tr}\sum_{m=1}^{\infty}\frac{1}{m}\int_{(n-1/2)\pi}^{(n+1/2)\pi} S^{2m}(\xi)d\xi, \tag{84}$$

where we defined

$$\Phi_n = \int_{(n-1/2)\pi}^{(n+1/2)\pi} \varphi(\xi)d\xi, \tag{85}$$

and $S(\xi)$ in Eq. (84) is the 2×2 S matrix defined in Eq. (74). With Eq. (77), we obtain the following explicit result for the roots of the spectral equation (70)

$$\xi_n = n\pi - \frac{\Phi_n}{\pi} - \frac{1}{\pi}\,\mathrm{Im}\sum_{m=1}^{\infty}\frac{(-1)^m}{m}\int_{(n-1/2)\pi}^{(n+1/2)\pi} R^m(\xi)e^{2mi\xi}d\xi, \tag{86}$$

where $R(\xi)$ is defined in Eq. (71). We can immediately check two important limits of Eq. (86). According to Figs. 1 and 4, for $d\to 0$ the step-in-the-box potential becomes an infinite square well. Therefore, in this limit, we expect $\xi_n = n\pi$. For $d=0$, we have $\gamma=0$ according to Eq. (35). In this case, the integrals in Eq. (86) can be performed trivially; they all vanish. Inspecting Eq. (80) for $\gamma=0$ shows that $\varphi(\xi)\equiv 0$, i.e., $\Phi_n=0$ for all n. Therefore, $\xi_n = n\pi$, as expected, which confirms the validity of Eq. (86) in the limit $d\to 0$.

Our second check concerns the case $d\to\infty$. In this case, with $\gamma\to\infty$ according to Eq. (35), the spectral equation (69) reduces to $\tan(\xi) = -1/\eta$, with the solution $\xi_n = n\pi - \arctan(1/\eta)$. Inspecting Eq. (86) when $\gamma\to\infty$, we see that again all the integrals in Eq. (86) vanish, but $\varphi(\xi) = \arctan(1/\eta)$ according to Eq. (80). According to Eq. (85), this means that $\Phi_n = \pi\arctan(1/\eta)$. All of these results used in Eq. (86) yield $\xi_n = n\pi - \arctan(1/\eta)$, the expected result in the case $d\to\infty$.

So far we have checked the two limits $\gamma\to 0$ and $\gamma\to\infty$, which check the average behavior of the roots of Eq. (69) including the phase Φ_n in Eq. (86). These limits, however, do not check the S-matrix terms in Eq. (86). According to Eq. (86), these terms are important for $\gamma\sim 1/(2n\pi)$, which allows for a large variation in the prefactor of the oscillating terms under the integral in Eq. (86), resulting in large contributions from these S-matrix terms.

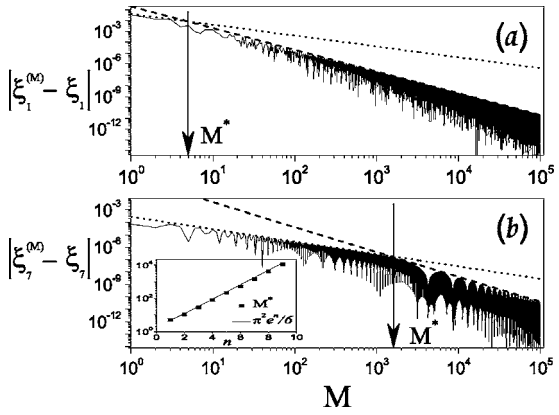

FIG. 8. The difference $|\xi_n^{(M)} - \xi_n|$ (solid lines), for fixed $\gamma = 1/(2\pi)$, $\eta = 3/(2\pi)$, for $n=1$ (a) and $n=7$ (b) as a function of M, where $\xi_n^{(M)}$ is computed using the first M terms in the m sum of Eq. (86), and ξ_n is the exact solution of the spectral equation (69) for $\gamma = 1/(2\pi)$ and $\eta = 3/(2\pi)$. $|\xi_n^{(M)} - \xi_n|$ (solid lines) decay according to $\sim 1/M$ (dotted lines) for $1 \le M \le M^*$. At $M \approx M^*$ (arrows) the $\sim 1/M$ behavior (dotted lines) crosses over to a $\sim 1/M^2$ behavior (dashed lines) which persists for at least up to $M = 10^5$, and probably to $M\to\infty$. The inset of panel (b) shows the crossover points M^* (solid squares) extracted from plots of $|\xi_n^{(M)} - \xi_n|$ for $n = 1, \ldots, 9$. The solid line in the inset is the theoretical estimate $M^*(n) = \pi^2 e^n/6$ (see text).

Therefore, as a test for Eq. (86), we choose $n=1$, $\gamma = 1/(2\pi)$, and $a/b = 3/4$, which yields $\eta = 3/(2\pi)$ and $v = 1 + 9/(4\pi^2)$. In this case, the first root of Eq. (69) is

$$\xi_1 = 2.475\,998\,479\,3\ldots. \tag{87}$$

Figure 8(a) shows $|\xi_1^{(M)} - \xi_1|$ (solid line), where $\xi_1^{(M)}$ is the first root of Eq. (69) computed using the first M terms of Eq. (86) and performing the integration over ξ numerically. Figure 8(a) shows that $|\xi_1^{(M)} - \xi_1| \sim 1/M^2$ (dashed line) over most of the M range shown in Fig. 8(a). Figure 8(b) shows $|\xi_7^{(M)} - \xi_7|$ (solid line) as a function of M. We see that an initial $\sim 1/M$ behavior (dotted line) crosses over to a $\sim 1/M^2$ behavior (dashed line) at $M^* \sim 1429$ (arrow). The crossover point M^* is determined as the intersection $M^* = A/B$ of the two functions A/M^2 (dashed line) and B/M (dotted line) fitted to $|\xi_7^{(M)} - \xi_7|$ (solid line). In a similar way, we extracted the crossover points M^* for $n = 1, \ldots, 6$ and $n = 8, 9$. Even for $n=1$, as shown in Fig. 8(a), although marginal, a crossover at $M^* \approx 5$ can be extracted. The inset in Fig. 8(b) shows $M^*(n), n = 1, \ldots, 9$ (solid squares) obtained graphically according to the procedure described above; they scale roughly exponentially in n.

For fixed γ and η [in the present case $\gamma = 1/(2\pi)$, $\eta = 3/(2\pi)$], the exponential scaling of M^* in n can be understood in the following way. We study the sum in Eq. (86), computing an estimate for its general term

$$J_{mn} = \frac{(-1)^m}{m} \int_{(n-1/2)\pi}^{(n+1/2)\pi} R^m(\xi) e^{2mi\xi} d\xi. \tag{88}$$

According to Eq. (81), we write it as

$$J_{mn} = \frac{1}{m} \int_{(n-1/2)\pi}^{(n+1/2)\pi} e^{2mi \arctan[\tanh(\gamma\xi)/\eta] + 2mi\xi} d\xi. \tag{89}$$

For small η and large n, we expand the arctan function in Eq. (89) to the first order to obtain

$$J_{mn} \approx \frac{(-1)^m}{m} \int_{(n-1/2)\pi}^{(n+1/2)\pi} e^{-2mi\eta[(1+e^{-2\gamma\xi})/(1-e^{-2\gamma\xi})] + 2mi\xi} d\xi. \tag{90}$$

Expanding the fraction in the exponent of Eq. (90) to first order in $e^{-2\gamma\xi}$, we obtain

$$J_{mn} \approx \frac{(-1)^m}{m} e^{-2mi\eta} \int_{(n-1/2)\pi}^{(n+1/2)\pi} e^{-4mi\eta e^{-2\gamma\xi} + 2mi\xi} d\xi. \tag{91}$$

Substituting $\xi = n\pi + y$, $-\pi/2 \leqslant y \leqslant \pi/2$, and expanding $e^{-2\gamma\xi}$ to first order in y, we obtain

$$J_{mn} \approx \frac{1}{m^2} \frac{\sin[4m\pi\gamma\eta e^{-2\gamma n\pi}]}{1 + 4\gamma\eta e^{-2\gamma n\pi}} e^{-2mi\eta[1+2e^{-2\gamma n\pi}]}. \tag{92}$$

For small m, the argument of the sine function is small. Linearizing the sine function in Eq. (92) shows that for small m the integrals $J_{mn} \sim 1/m$. The monotonically rising behavior of the sine function in Eq. (92) changes to an oscillatory behavior when its argument crosses $\pi/2$. This happens at

$$m^* = \frac{1}{8\gamma\eta} e^{2\gamma\pi n}. \tag{93}$$

For $m > m^*$, the integrals J_{mn} behave like $\sim 1/m^2$ on average.

We now argue, but cannot formally prove, that the qualitative change in the m behavior of J_{mn} reflects itself in a qualitative change in the behavior of the sum in Eq. (86) as a function of M, with the crossover between $\sim 1/M$ and $\sim 1/M^2$ behavior occurring at $M^* \approx m^*$. Thus, according to Eq. (93), we predict an exponential scaling of M^* in n, which in our case ($\gamma = 1/2\pi$, $\eta = 3/2\pi$ fixed) takes the form

$$M^*(n) = \frac{\pi^2}{6} e^n. \tag{94}$$

The solid line in the inset of Fig. 8(b) shows this scaling function. There is good agreement between the graphically extracted crossover points M^* [full squares in Fig. 8(b)] and the prediction (94). Since asymptotically (for large M) all $|\xi_n^{(M)} - \xi_n| \sim 1/M^2$, we conclude that (i) $\xi_n^{(M)}$ converges to the exact value ξ_n, and (ii) the algebra leading us to Eq. (86) is correct.

We are now going to derive an integral-free representation of ξ_n based on Newtonian orbits, ghost orbits, and specters. We start with the phase factor $\varphi(\xi)$ defined in Eq. (80) and write it as

$$\varphi(\xi) = \arctan\left[\frac{1}{\eta}\left(\frac{1 - e^{-2\gamma\xi}}{1 + e^{-2\gamma\xi}}\right)\right]. \tag{95}$$

We recognize immediately that this phase factor is due to ghost orbits that travel entirely under the potential barrier in $a \leqslant x \leqslant b$ (see Fig. 1). This is so since the exponential factor in Eq. (95) can be written as $e^{iS_g(\xi)}$, where $S_g(\xi) = 2i\gamma\xi$ is the classical action of an under-barrier specter. Using formula 4.4.28 of Ref. [34], viz.,

$$\arctan(x) = \frac{i}{2} \ln\left(\frac{i + x}{i - x}\right), \tag{96}$$

we transform Eq. (95) into

$$\varphi(\xi) = \frac{i}{2} \ln\left[\frac{i\eta + 1}{i\eta - 1}\right] + \frac{i}{2} \ln\left[\frac{1 - re^{-2\gamma\xi}}{1 - r^* e^{-2\gamma\xi}}\right]. \tag{97}$$

Since both arguments of the ln functions in Eq. (97) are unimodular phase factors, we obtain

$$\varphi(\xi) = \arctan\left(\frac{1}{\eta}\right) - \mathrm{Im} \ln[1 - re^{-2\gamma\xi}]. \tag{98}$$

Using the series expansion of the ln function (see, e.g., Ref. [31] formula 1.511), viz.,

$$\ln(1 - x) = -\sum_{\nu=1}^{\infty} \frac{1}{\nu} x^\nu, \tag{99}$$

we obtain the final result for $\varphi(\xi)$ in the form

$$\varphi(\xi) = \arctan\left(\frac{1}{\eta}\right) + \mathrm{Im} \sum_{\nu=1}^{\infty} \frac{1}{\nu} r^\nu e^{i\nu(2i\gamma\xi)}. \tag{100}$$

Formula (100) has an immediate and direct interpretation in terms of periodic orbits. The first term in Eq. (100) is a constant phase factor, which corresponds to "orbits of zero length" [3]. The sum in Eq. (100) is over the under-barrier ghost orbits oscillating ν times from $x = a$ to $x = b$ and back to $x = a$. The primitive ghost with action $2i\gamma\xi$ is coded with the symbol $\mathcal{R}$. It corresponds to the specter P_6 (see Fig. 1). Its νth repetition with action $2\nu i\gamma\xi$ is coded by ν symbols $\mathcal{R}$,

$$\underbrace{\mathcal{R}\mathcal{R}\cdots\mathcal{R}}_{\nu \text{ times}},$$

i.e., $\mathcal{R}^\nu$. Since their actions, appearing in the exponent of Eq. (100), are purely imaginary, and since they never emerge from under the potential barrier, they are specters, too.

The amplitude factor r^ν in Eq. (100), corresponding to the specter $\mathcal{R}^\nu$, has a straightforward physical interpretation. The specter $\mathcal{R}^\nu$ bounces ν times between the step at $x = a$ and the wall at $x = b$, picking up a phase factor -1 for each bounce at the wall, and a phase factor $-r$ for each reflection off the step at $x = a$. Altogether, this results in an amplitude factor r^ν as shown in Eq. (100). Based on Eq. (100), we can now provide an integral-free, periodic-orbit expansion for the phase Φ_n in Eq. (86). Term-by-term integration of Eq. (100) yields

$$\Phi_n = \pi \arctan\left(\frac{1}{\eta}\right) + \mathrm{Im} \sum_{\nu=1}^{\infty} \frac{r^\nu}{\gamma \nu^2} e^{-2n\nu\gamma\pi} \sinh(\nu\gamma\pi). \tag{101}$$

To obtain Eq. (101), we must exchange the order of integration and summation, which is allowed in this case since the sum in Eq. (100) converges absolutely [35].

We now turn to the sum in Eq. (86). Expanding $R^m(\xi)$ into a power series in $e^{-2\gamma\xi}$,

$$R^m(\xi) = r^m \left[\frac{1 - r^* e^{-2\gamma\xi}}{1 - r e^{-2\gamma\xi}}\right]^m = \sum_{\nu=0}^{\infty} A_\nu^{(m)} e^{-2\nu\gamma\xi}, \tag{102}$$

we see that the terms under the integral in Eq. (86) correspond to the Newtonian orbit $\mathcal{L}^m$ with action $2m\xi$ (for $\nu=0$) and all possible ghost orbits with complex actions $2m\xi + 2i\nu\gamma\xi$, which can be combined from m Newtonian traversals (back and forth) between $x=0$ and $x=a$, and $\nu = 1, 2, \ldots, \infty$ under-barrier traversals (back and forth) between $x=a$ and $x=b$. Substituting the series (102) into Eq. (86) and performing the integrals, we obtain the following integral-free, periodic-orbit expansion for the roots ξ_n of the spectral equation (69)

$$\xi_n = n\pi - \arctan\left(\frac{1}{\eta}\right) - \frac{1}{\pi} \mathrm{Im} \sum_{\nu=1}^{\infty} \frac{r^\nu}{\gamma \nu^2} e^{-2n\nu\gamma\pi} \sinh(\nu\gamma\pi)$$
$$- \frac{1}{\pi} \mathrm{Im} \sum_{m=1}^{\infty} \frac{1}{m} \sum_{\nu=1}^{\infty} \frac{A_\nu^{(m)}}{\nu\gamma - im} e^{-2n\nu\gamma\pi} \sinh(\nu\gamma\pi). \tag{103}$$

There are three different ways of expressing the coefficients $A_\nu^{(m)}$. According to their definition (102), they are given by

$$A_\nu^{(m)} = r^m \frac{1}{\nu!} \frac{d^\nu}{dx^\nu} \left[\frac{1 - r^* x}{1 - r x}\right]^m \Bigg|_{x=0}. \tag{104}$$

The expression (104), although formally correct, is not very useful. Using the binomial theorem gives a more useful, explicit formula

$$A_\nu^{(m)} = \frac{1}{m} (-1)^{m+\nu} \sum_{\mu=0}^{\min[m,\nu]} \left(\frac{r^*}{r}\right)^\mu \binom{m}{\mu} \binom{-m}{\nu - \mu}. \tag{105}$$

The most useful representation for the $A_\nu^{(m)}$ coefficients, however, is their expansion in terms of periodic orbits. We obtain

$$A_\nu^{(m)} = \sum_{\substack{\hat{w} \\ l(\hat{w}) = m+\nu \\ \hat{w} = \lambda \hat{w}_p}} \frac{1}{\lambda} \left[(-1)^{\hat{\chi}(\hat{w}_p)} r^{\hat{\alpha}(\hat{w}_p)} t^{\hat{\beta}(\hat{w}_p)}\right]^\lambda. \tag{106}$$

In Eq. (106), the sum is over all binary necklaces $\hat{w}$ of length $m+\nu$, where $\hat{w}$ can be written as a repetition of λ identical, shorter pieces $\hat{w}_p$. The functions $\hat{\chi}$, $\hat{\alpha}$, and $\hat{\beta}$ in Eq. (106) are the necklace analogues of the word functions (33).

Equation (103) combined with Eq. (106) is the central result of our work. It is an advance over Eq. (86) for two reasons: (i) There is still an integral in Eq. (86), but the set of equations (103) and (106) is explicit, i.e., free of all integrals. (ii) The physics is much more transparent in Eqs. (103) and (106). For instance, reflection and transmission coefficients, r and t, respectively, appear explicitly in Eq. (106), and all contributing periodic orbits, including the ghost orbits, are enumerated explicitly, one by one.

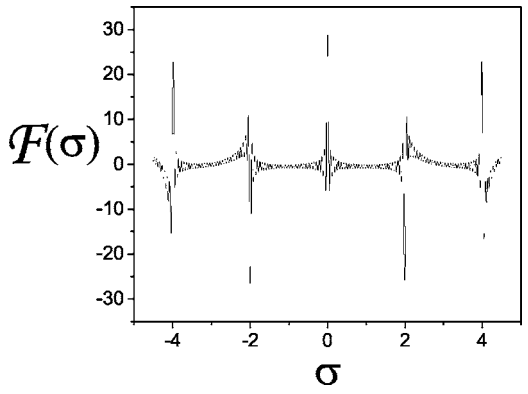

FIG. 9. Fourier transform $\mathcal{F}^{(N=30)}(\sigma) = \sum_{n=1}^{N=30} \cos(\sigma\xi_n)$ of the first $N=30$ roots ξ_n of the spectral equation (69). It is sharply peaked at $\sigma = 0, \pm 2, \pm 4, \ldots$. The smooth background in $\mathcal{F}^{(N=30)}(\sigma)$ is due to ghost orbits. The rapid oscillations are a finite-sample effect since $N=30$ is finite.

V. EXTRACTING GHOST ORBIT INFORMATION

Up to this point, we have computed energy levels in terms of periodic orbits. In this section, we invert this procedure to show that given a set of energy levels $\{\xi_n\}_{n=1}^N$, it is possible to extract periodic-orbit information from them, in particular information on the periodic ghost orbits. We define the Fourier transform of the level density $\rho^{(N)}(\xi) = \sum_{n=1}^N \delta(\xi - \xi_n)$ according to

$$\mathcal{F}^{(N)}(\sigma) = \mathrm{Re} \int_{0^+}^{\xi_{max}} \rho(\xi) e^{-i\sigma\xi} d\xi = \sum_{n=1}^{N} \cos(\sigma\xi_n), \tag{107}$$

where $\xi_N < \xi_{max} < \xi_{N+1}$ and 0^+ means that we do not include the level $\xi_0 = 0$ in the Fourier transform (107). We denote by $\mathcal{F}(\sigma)$ the $N \to \infty$ limit of $\mathcal{F}^{(N)}(\sigma)$. According to its definition, $\mathcal{F}(\sigma)$ is an even function of σ, i.e., $\mathcal{F}(-\sigma) = \mathcal{F}(\sigma)$. To illustrate the overall structure of $\mathcal{F}(\sigma)$, we computed $\mathcal{F}^{(N=30)}(\sigma)$ for the case $v = 1.02$ and $a/b = 3/4$. The result, displayed in Fig. 9, shows that $\mathcal{F}(\sigma)$ consists of an array of peaks with spacing $\Delta\sigma = 2$ that grow out of a smooth background. We explain the peaks as follows. According to Eq. (103), the average behavior of ξ_n is

$$\xi_n \sim n\pi - \arctan\left(\frac{1}{\eta}\right) \tag{108}$$

for large n. Fourier transforming Eq. (108) according to Eq. (107) results in (Ref. [31] formulas 1.3421 and 1.3422)

$$\mathcal{F}^{(N)}(\sigma) = \left\{ -\frac{1}{2} + \frac{\sin\left[\left(N+\frac{1}{2}\right)\pi\sigma\right]}{2\sin\left(\frac{\pi\sigma}{2}\right)} \right\} \cos\left[\sigma \arctan\left(\frac{1}{\eta}\right)\right] + \left\{ \frac{\sin\left[\left(\frac{N+1}{2}\right)\sigma\pi\right]\sin\left[\frac{N\sigma\pi}{2}\right]}{\sin\left(\frac{\sigma\pi}{2}\right)} \right\} \times \sin\left[\sigma \arctan\left(\frac{1}{\eta}\right)\right]. \quad (109)$$

This function is sharply peaked at $\sigma = 0, \pm 2, \pm 4, \ldots$, which explains the sharp peaks in Fig. 9, including their location. Since for our choice of parameters $\cos[2\arctan(1/\eta)] < 0$ ($\cos[4\arctan(1/\eta)] > 0$), Eq. (109) also explains why $\mathcal{F}^{(N=30)}(\sigma)$ is sharply negative (positive) at $\sigma \approx \pm 2$ ($\sigma \approx \pm 4$). The term $\sim \sin[\sigma \arctan(1/\eta)]$ in Eq. (109) explains the slight asymmetry in $\mathcal{F}^{(N=30)}(\sigma)$ at $\sigma \approx \pm 2, \pm 4$. For large N and in the vicinity of $\sigma = 0$, we have

$$\mathcal{F}(\sigma) \to \delta(\sigma) - \frac{1}{2}. \quad (110)$$

To investigate further the structure of $\mathcal{F}(\sigma)$, we use Eq. (77) to write Eq. (83) as

$$\mathcal{N}(\xi) = -\frac{1}{2} + \frac{\xi}{\pi} + \frac{\varphi(\xi)}{\pi} + \frac{1}{\pi} \mathrm{Im} \sum_{m=1}^{\infty} \frac{(-1)^m}{m} R^m(\xi) e^{2im\xi}. \quad (111)$$

We obtain the level density $\rho(\xi)$ from ξ by differentiation,

$$\rho(\xi) = \frac{d\mathcal{N}(\xi)}{d\xi} = \frac{1}{\pi} + \frac{\varphi'(\xi)}{\pi} + \frac{1}{\pi} \mathrm{Im} \sum_{m=1}^{\infty} (-1)^m [R^{m-1}(\xi) R'(\xi) + 2iR^m(\xi)] e^{2im\xi}. \quad (112)$$

Using Eq. (112) in Eq. (107), we obtain a physical interpretation of the peaks at $\sigma = \pm 2, \pm 4, \ldots$ as due to the oscillating terms in the sum of Eq. (112), since, because of the imaginary part in Eq. (112), both $e^{2im\xi}$ and $e^{-2im\xi}$ terms appear and contribute to $\mathcal{F}(\sigma)$ peaks located at $\sigma = \pm 2m$. These terms are produced by orbits that oscillate (back and forth) m times between $x = 0$ and $x = a$, and an arbitrary number of times between $x = a$ and $x = b$.

The peak at $\sigma = 0$ is special. According to Eq. (112), this peak is produced by the nonoscillating terms $1/\pi + \varphi'(\xi)/\pi$, where the former is responsible for the δ-function part of the structures in $\mathcal{F}(\sigma)$ at $\sigma = 0$, and the latter is responsible for the background, assuming that the background features produced by the $m = 1, \ldots, \infty$ terms in Eq. (112) have died away at $\sigma = 0$. Figure 9 shows that this is a good approximation. Realizing that according to Eq. (100), $\varphi(\xi)$ contains contributions from the specters $\mathcal{R}^\nu$, $\nu = 1, 2, \ldots, \infty$, we will focus on $\mathcal{F}(\sigma)$ in the vicinity of $\sigma = 0$ to extract ghost orbit information from the Fourier transform $\mathcal{F}(\sigma)$, and by implication, from the energy levels ξ_n. In particular, we want to extract the constant γ, which determines the classical actions of the specters.

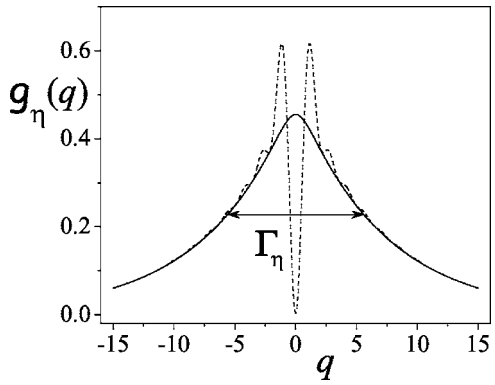

FIG. 10. Full line: Scaling function $g_\eta(q)$ used for extracting the reduced action of specters from numerical or experimental spectral data. Dashed line: Regularized Fourier transform $f^{(N)}(\sigma = q\gamma)$ for $N = 30$.

Near $\sigma = 0$, the factor $1/\pi$ in the level density (112) produces the function $\delta(\sigma) - 1/2$ in $\mathcal{F}(\sigma)$. The term $-1/2$ prevents us from counting the unphysical level $\xi_0 = 0$, which does not correspond to a physical state; the term $-1/2$ also appears in Eqs. (109) and (110). Since no ghost information is contained in the term $\delta(\sigma) - 1/2$, we subtract it from $\mathcal{F}(\sigma)$ and study the regularized Fourier transform

$$f(\sigma) = \mathcal{F}(\sigma) - \delta(\sigma) + \frac{1}{2} \quad (113)$$

in the vicinity of $\sigma = 0$. According to Eq. (112), $f(\sigma)$ is given explicitly by

$$f(\sigma) = \frac{1}{\pi} \int_{0^+}^{\xi_{max}} \varphi'(\xi) \cos(\sigma\xi) d\xi. \quad (114)$$

Since the integrand in Eq. (114) is a smooth function, we may replace $0^+ \to 0$. Moreover, for large ξ_{max}, we may replace ξ_{max} by ∞ to obtain

$$f(\sigma) = g_\eta(\sigma/\gamma) \quad (115)$$

with the scaling function

$$g_\eta(q) = \frac{\eta}{\pi} \int_0^\infty \frac{\cos(qz)}{\sinh^2(z) + \eta^2 \cosh^2(z)} dz. \quad (116)$$

The full line in Fig. 10 shows it for $v = 1.02$ ($\eta = \sqrt{2}/10$). Its full width at half maximum (FWHM) is denoted by Γ_η.

Since $\Sigma_{n=1}^{\infty} \cos(\sigma n\pi) = \delta(\sigma) - 1/2$ in the vicinity of $\sigma = 0$, we define the finite-N approximation, $f^{(N)}(\sigma)$, of the regularized Fourier transform (113) according to

$$f^{(N)}(\sigma) = \sum_{n=1}^{N} [\cos(\sigma\xi_n) - \cos(\sigma n\pi)] u(\xi_n), \quad (117)$$

where $u(\xi_n)$ is a weight function that suppresses the Gibbs phenomenon [14,36]. Since $q = \sigma/\gamma$ and $f(\sigma) = g_\eta(q)$, we expect that $f^{(N)}(\sigma = q\gamma)$ is close to the scaling function $g_\eta(q)$. The dashed line in Fig. 10 shows $f^{(N)}(\sigma = q\gamma)$ for the case

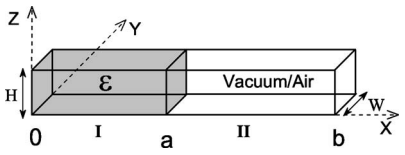

FIG. 11. Setup of the proposed quasi-one-dimensional microwave experiment for extracting ghost orbit information from experimental resonance spectra. Coupling the width W of the cavity to the microwave frequency ω allows scaled spectra to be taken in the tunneling regime.

$v=1.02$ ($\eta=\sqrt{2}/10$) for $N=30$ and $u(\xi)=\cos^2[\xi\pi/(2\xi_N)]$. As expected, $f^{(30)}$ is close to g_η, especially in the wings (for large $|q|$), but shows oscillations that are most pronounced in the vicinity of $q=0$. We checked that the oscillations are due to the finite size of the sample of levels (here $N=30$), and that the oscillations are pushed to an ever smaller interval around $q=0$ for $N\to\infty$.

Figure 10 shows that, the oscillations notwithstanding, the excellent agreement between $f^{(N)}(\sigma=q\gamma)$ and $g_\eta(q)$ for large $|q|$ allows us to extract the width Γ_η from $f^{(N)}$ obtained from N numerically computed, or experimentally measured, energy levels.

The procedure is the following. For given η, which is determined by the model system or by the experimental setup (see Sec. VI), (i) plot the scaling function $g_\eta(q)$; (ii) determine the FWHM Γ_η of $g_\eta(q)$; (iii) plot $f^{(N)}(\sigma)$; (iv) determine the FWHM Γ_N of $f^{(N)}(\sigma)$; and finally (v) compute $\gamma^{(\mathrm{num,expt})}$ according to

$$\gamma^{(\mathrm{num,expt})}=\frac{\Gamma_N}{\Gamma_\eta}. \tag{118}$$

In Sec. VI, we propose an experiment which should allow (i) experimental verification of ghost orbits in the tunneling regime and (ii) measurement of their properties using the above scheme for determining $\gamma^{(\mathrm{expt})}$.

VI. EXPERIMENT

This section proposes an experimental implementation of the scaling step-in-the-box potential that allows realization of the three energy regimes $E>V_0$ (above barrier), $E=V_0$ (critical), and $E<V_0$ (tunneling). Figure 11 shows a setup consisting of a quasi-one-dimensional (q1D), dielectric-loaded microwave cavity of width W, height H, and total length b. Both H and W are assumed to be small compared with the cavity's length b. Region I of the cavity ($0<x<a$) is filled with a low-loss, dielectric substance of relative permittivity $\kappa_e=\epsilon/\epsilon_0>1$, where ϵ (ϵ_0) is the permittivity of the substance (vacuum). We assume that the magnetic permeability μ of the substance differs negligibly from μ_0, the magnetic permeability of the vacuum. This ensures that the electromagnetic boundary conditions are the same as the ones of the scaling Schrödinger equation. For calculations below, we assume that vacuum ($\kappa_e=1$, $\mu=\mu_0$) fills region II ($a<x<b$) of the cavity, although all computations below are affected little if air ($\kappa_e\approx 1$, $\mu\approx\mu_0$) fills region II. We also assume that the cavity height H is small compared with $\lambda_{min}/2$, where λ_{min} is the smallest wavelength occurring in the cavity for any of the operating frequencies used in the experiment. Since the relative dielectric constant $\kappa_e>1$ in region I, the smallest wavelengths occur there and we require

$$H<\frac{c\pi}{\omega_{max}\sqrt{\kappa_e}}, \tag{119}$$

where c is the speed of light in vacuum and ω_{max} is the largest microwave frequency used in the experiment. If the criterion (119) is fulfilled, only transverse magnetic (TM) modes [37], TM_{nm0}, occur in the cavity, where n,m are the mode indices in the x and y directions, respectively, and "0" indicates that the electric field $\vec{\mathcal{E}}$ inside the cavity is constant in the z direction. The electric field $\vec{\mathcal{E}}$ of a TM_{nm0} mode points into the z direction, $\vec{\mathcal{E}}=\mathcal{E}_z\hat{z}$, and in addition, $\mathcal{E}_z$ depends only on the two spatial dimensions x and y, i.e., $\mathcal{E}_z=\mathcal{E}_z(x,y)$.

To implement the one-dimensional scaling potential $V_s(x)$ specified in Eqs. (1) and (5), we focus on the TM_{n10} modes of the cavity shown in Fig. 11. In this case, the electric field component $\mathcal{E}_z$ has the form

$$\mathcal{E}_z^{(n)}(x,y)=A_n\psi_n(x)\sin(\pi y/W), \tag{120}$$

where A_n is a constant. Since $\mathcal{E}_z^{(n)}(x,y)$ satisfies the Helmholtz equation [37]

$$\left[\Delta+\frac{\kappa\omega^2}{c^2}\right]\mathcal{E}_z^{(n)}(x,y)=0, \tag{121}$$

where $\kappa=\kappa_e$ in region I and $\kappa=1$ in region II, we have

$$\psi_n''(x)-\left(\frac{\pi}{W}\right)^2\psi_n(x)+\frac{\kappa\omega^2}{c^2}\psi_n(x)=0. \tag{122}$$

To ensure that only TM_{n10} modes are excited in the cavity, the width W of the cavity must be between one half and one wavelength of the microwave field for all operating conditions in region I. This condition requires

$$\frac{\pi c}{\omega\sqrt{\kappa_e}}<W<\frac{2\pi c}{\omega\sqrt{\kappa_e}}. \tag{123}$$

Our aim now is to turn Eq. (122) into an energy-scaling Schrödinger equation such that its potential corresponds to the energy-scaling step-in-the-box potential (1) with $V_0=vE$ and v a constant. We accomplish this by assuming that the width W of the cavity is coupled to the cavity frequency via

$$W=\frac{s}{\omega}, \tag{124}$$

where s is constant. The W scaling (124) together with the estimate (123) yields the following condition for s

$$\frac{\pi c}{\sqrt{\kappa_e}}<s<\frac{2\pi c}{\sqrt{\kappa_e}}. \tag{125}$$

We now define

$$E = \frac{\omega^2}{c^2}\left[\kappa_e - \left(\frac{\pi c}{s}\right)^2\right], \tag{126}$$

which turns Eq. (122) into the energy-scaling Schrödinger equation

$$-\psi_n''(x) + V(E_n;x)\psi_n(x) = E_n\psi_n(x), \tag{127}$$

where

$$V(E;x) = \begin{cases} 0, & \text{in region I,} \\ vE, & \text{in region II} \end{cases} \tag{128}$$

and

$$v = \frac{(\kappa_e - 1)}{\kappa_e - (\pi c/s)^2} \tag{129}$$

is the scaling constant of the potential. Judicious adjustment of s allows realization of all three energy regimes, $E > V_0$ $(v < 1)$, $E = V_0$ $(v = 1)$, and $E < V_0$ $(v > 1)$.

We focus now on the tunneling case $E < V_0$. Section V showed that the reduced action γ of the specters can be extracted reliably from 30 energy levels. In the microwave language of this section, this means that the cavity setup should be able to provide 30 TM_{n10} microwave resonances ω_n without excessive demands on the required microwave frequencies or cavity dimensions. To show that this is possible, we give next the dimensions for an actual experiment.

A reasonable choice for κ_e is $\kappa_e = 2$, approximately the value for many liquid and solid substances [38]. Moreover, successful experiments with dielectric-loaded microwave cavities were already performed with paraffin wax, $\kappa_e \simeq 2.2$ [12,13] and Teflon, $\kappa_e \simeq 2.08$ [14]. To remain close to the example of Sec. V, we choose $v = 1.02$. With $\kappa_e = 2$ and $v = 1.02$ chosen, we may now compute the constant s that relates the microwave frequency ω to the cavity's width W. Solving Eq. (129) gives, to two-digit accuracy,

$$s \approx 0.99\pi c. \tag{130}$$

Note that s in Eq. (130) satisfies the condition (125). A crude approximation of the energy eigenvalues E_n of Eq. (127) is the infinite-box limit

$$E_n = \left(\frac{n\pi}{a}\right)^2. \tag{131}$$

Equation (126) gives the corresponding resonance frequencies $\nu_n = \omega_n/2\pi$, where

$$\nu_n = n\frac{0.505c}{a}. \tag{132}$$

If we choose $a = 1$ m, which is approximately a cavity dimension used in a recent, successful microwave experiment [12,13], we obtain

$$\nu_1 \approx 150 \text{ MHz}, \quad \nu_{30} \approx 4.54 \text{ GHz}, \tag{133}$$

convenient values for microwave equipment [12,13]. It remains to compute the width W of the cavity for ν_1 and ν_{30}. With s of Eq. (130), we obtain, to two-digit accuracy,

$$W_1 = 99 \text{ cm}, \quad W_{30} = 3.3 \text{ cm}. \tag{134}$$

These are convenient dimensions for experimental work.

Our proposed q1D microwave setup resembles quasi-two-dimensional (q2D), flat microwave cavities already used successfully for quantum chaos studies [24]. Quasi-2D microwave cavities were first used by Stöckmann and Stein [36], and Sridhar and collaborators [39,40] for the study of spectral statistics and wave functions [3]. Later, dielectric-loaded q2D cavities were used for the investigation of non-Newtonian orbits [14] and an experimental test [12,13] of a predicted [11] universal correction to the Weyl formula [3] of ray-splitting systems [8–15]. The use of q2D cavities is a mature technology, making the experiments proposed in this section eminently feasible.

When we cast the Helmholtz equation of a dielectric-loaded cavity into the form of an equivalent Schrödinger equation, the potential V is automatically scaling in $E \sim \omega^2$ for q2D cavities [11–14]; for our proposed q1D cavity it is not. This explains why we must introduce a cavity with variable width W according to Eq. (124). Although a cavity with a movable boundary has been used already to measure parametric correlation of energy levels in a Sinai ray-splitting billiard [41], the variable width we propose introduces the complication of keeping the width of a dielectric insert equal to the cavity width W. Though this presents some experimental challenges, we propose two methods to facilitate experimental implementation of a dielectric with variable width.

The most straightforward way would use a nonconducting, dielectric liquid. Standing the q1D cavity on end solves the problem of keeping the liquid confined to region I of the cavity; the dimension of any meniscus will be much smaller than the wavelength and, therefore, of no consequence. Use of liquid dielectrics has an additional advantage: mixtures of liquids allow κ_e to be adjusted continuously, in case this turns out to be necessary.

A second method would be to slice a solid dielectric of length a, height H, and width ~ 1 m into, say, $M = 1000$, or more, thin slices of width $w \sim 1$ mm, or less. Adding slices to, or removing slices from a stack of width W corresponds to discretizing the width W of the dielectric in steps of w according to $W_j = jw$, $j = 1, \ldots, M$. Taking a complete microwave spectrum ω_n, $n = 1, \ldots, N$ for each width W_j of the stack allows construction of a two-dimensional map of ω_n versus W_j. Interpolating this map, we would obtain the smooth functions $\omega_n(W)$, $n = 1, \ldots, N$. Intersecting $\omega_n(W)$ with the smooth curve $\omega = s/W$ yields the scaled resonances $\omega_n^{(s)}$, $n = 1, \ldots, N$ $(N \approx 30)$, needed for extracting the ghost orbit information according to the procedure outlined in Sec. V.

VII. DISCUSSION

As the energy is lowered, a classical orbit that for $E > V_0$ propagates freely in region II $(a < x < b)$ of the step-in-the-box potential (see Fig. 1) becomes a ghost orbit for $E < V_0$ if any part of the orbit has an overlap with region II. In this picture, the below-barrier case does not seem so different from the above-barrier case, and one might be tempted to

develop a tunneling theory for the step-in-the-box potential by simply allowing the actions of the classical orbits to become complex, otherwise keeping all the formulas developed in Sec. III unmodified. We call this procedure the complexification approach. Complexification is intuitively appealing since it would allow us to develop a unified theory of both the above-barrier regime and the tunneling regime. Dabaghian and Jensen [22] recently used complexification to compute energy levels for a nonscaling step-in-the-box potential. However, as discussed below, there are problems with this approach.

For $E<V_0$ complexification starts with the S matrix (40). For $E<V_0$, the matrix $S(\xi)$ turns into the 4×4 complex, nonunitary matrix

$$\hat{S}(\xi)=\begin{pmatrix} 0 & \hat{r}e^{i\hat{u}_+\xi} & \hat{t}e^{i\hat{u}_+\xi} & 0 \\ -e^{i\hat{u}_+\xi} & 0 & 0 & 0 \\ 0 & 0 & 0 & -e^{i\hat{u}_-\xi} \\ 0 & \hat{t}e^{i\hat{u}_-\xi} & -\hat{r}e^{i\hat{u}_-\xi} & 0 \end{pmatrix}, \tag{135}$$

where

$$\hat{r}=\frac{1-i\eta}{1+i\eta}, \quad \hat{t}^2=1-\hat{r}^2,$$

$$\hat{u}_+=\frac{(1+\hat{\omega})}{2}, \quad \hat{u}_-=\frac{(1-\hat{\omega})}{2},$$

$$\hat{\omega}=\frac{1-\hat{\gamma}}{1+\hat{\gamma}}, \quad \hat{\gamma}=\frac{i\eta d}{a}, \quad \eta=\sqrt{v-1}. \tag{136}$$

Indeed, $\det[\hat{S}(\xi)-1]=0$ yields the correct spectral equation (66). The matrix (135) is now used directly in Eq. (50) to obtain the staircase function in the below-barrier case according to

$$\hat{\mathcal{N}}(\xi)=-\frac{1}{2}+\frac{\xi}{\pi}+\frac{1}{2\pi}\,\mathrm{Im\,Tr}\sum_{m=1}^{\infty}\frac{1}{m}\hat{S}^{2m}(\xi), \tag{137}$$

where we used the vanishing of the trace of the odd powers of $\hat{S}(\xi)$. The staircase function $\hat{\mathcal{N}}(\xi)$ obtained by using the first ten terms in the sum in Eq. (137) is shown in Fig. 12. We see that $\hat{\mathcal{N}}(\xi)$ is highly oscillatory in certain ξ intervals. Including more than ten terms in the sum (137) shows that $\hat{\mathcal{N}}(\xi)$ actually diverges to infinity in the ξ intervals in which $\hat{\mathcal{N}}(\xi)$ shows oscillations in Fig. 12. Therefore, the complexified $\hat{\mathcal{N}}(\xi)$ is an unsatisfactory starting point for the computation of energy levels ξ_n in the below-barrier regime. For comparison, Fig. 12 also shows $\mathcal{N}(\xi)$ computed according to Eq. (111), which is based on the unitary theory derived in this paper (dashed line in Fig. 12), again using the first ten terms in the sum. Now $\mathcal{N}(\xi)$ is much closer to a staircase function.

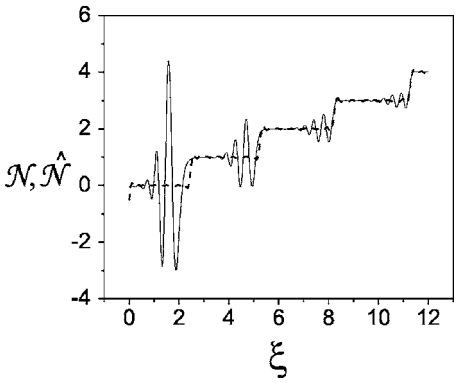

FIG. 12. Staircase functions $\hat{\mathcal{N}}(\xi)$ (solid line) computed with the 4×4 complexification approach and $\mathcal{N}(\xi)$ (dashed line) computed with the 2×2 unitary S-matrix approach. The large oscillations in $\hat{\mathcal{N}}(\xi)$ become worse as more periodic orbits are included. Thus $\hat{\mathcal{N}}(\xi)$ diverges.

The numerically observed convergence of $\mathcal{N}(\xi)$ is not surprising, since the algebra leading to Eq. (111) is exact. The expression for $\hat{\mathcal{N}}(\xi)$, on the other hand, is not derived, but obtained by unjustified, analytic continuation without rigorous derivation. There is no *a priori* reason for why this procedure should work. Indeed, as we saw above, it fails.

The reason for the divergences of $\hat{\mathcal{N}}(\xi)$ is the occurrence of eigenvalues Λ of $\hat{S}(\xi)$ with $|\Lambda|>1$ in certain ξ intervals. Use of an S matrix with $|\Lambda|>1$ in Eq. (137) leads to an $\hat{\mathcal{N}}$ that diverges exponentially in M, where M is the number of terms included in the sum over m in Eq. (137). We conclude that due to the occurrence of S-matrix eigenvalues Λ with $|\Lambda|>1$, the direct complexification attempted in Ref. [22] yields divergent results while our unitary 2×2 theory yields exact, convergent periodic-orbit expansions of the energy eigenvalues of the step-in-the-box potential. The tunneling theory we presented in this paper completes the task of the analytical solution of the step-in-the-box potential in all energy regimes.

One might argue that the observed, divergent behavior of $\hat{\mathcal{N}}(\xi)$ is due to our use of a scaling theory. However, direct investigation of the nonscaling case treated in Ref. [22] revealed similar divergences [28], again due to S-matrix eigenvalues whose modulus exceeds 1.

Still, when analyzed term-by-term, the complexified, nonunitary 4×4 S matrix yields the correct amplitudes for each periodic (ghost) orbit contributing to the staircase (50). In this light, the divergence of the 4×4 theory is puzzling until one realizes that, although the 2×2 and the 4×4 theories, respectively, include the same orbits with the same amplitudes, the two theories imply a different order of summation. While the 4×4 theory sums the orbits according to their number of encounters with the step at $x=a$ (which is correct for $E>V_0$, but incorrect for $E<V_0$), the 2×2 theory implies that for each bounce off (transmission through) the left-hand side of the step, all trajectories with an arbitrary number of bounces off the right-hand side have to be summed *first*. Expressed symbolically, if $\{\hat{w}\}$ are necklaces consisting of m symbols $\mathcal{L}$ and n symbols $\mathcal{R}$, then one *first* has to sum over

n, and *then* sum over *m*. Thus, the step-in-the-box potential provides an illustrative case of Riemann's reordering theorem [28] according to which, as is the case here, a nontrivial reordering of the terms of a conditionally convergent sum can lead to different (including divergent) results.

Though it is one-dimensional, the step-in-the-box potential is not trivial. We showed that all periodic orbits contributing to the periodic-orbit expansions can be labeled one-to-one with the help of binary necklaces. However, since there are $\sim 2^m/m$ binary necklaces of length m [33] (for m prime), the number of periodic orbits contributing to our periodic-orbit expansions grows exponentially, and we emphasize that in the tunneling regime, the majority in this exponential proliferation are ghost orbits. Thus, in the tunneling regime, periodic ghost orbits outnumber Newtonian orbits.

An exponentially growing number of periodic orbits is a hallmark of quantum chaotic systems. Is our one-dimensional step-in-the-box potential quantum chaotic? We argue no, since the step-in-the-box potential is not classically chaotic. The reason is the following: While satisfying a necessary condition for classical chaos, i.e., the exponential proliferation of periodic orbits, it does not satisfy the more important, sufficient condition: a positive Liapunov exponent. In fact, since the step-in-the-box potential is conservative and one-dimensional, its Liapunov exponent is zero [3].

However, the step-in-the-box potential mimics a classically chaotic system with a positive Liapunov exponent in the following way. A quantum particle approaching the step has to make a choice: to reflect or to transmit. The corresponding *classical ray dynamics* are probabilistic [10]. Thus, the resulting particle trajectories may look complicated, mimicking a chaotic trajectory. But since this "chaos" is generated by true randomness, not the *deterministic* randomness of dynamics with a positive Liapunov exponent, it is not appropriate to call the step-in-the-box potential quantum chaotic. We prefer, instead, to call it quantum stochastic [21].

Although our paper focuses on the case of a single step in a box with infinitely high walls, it is possible to generalize the theory to piecewise constant potentials, and potentials consisting of arrays of δ functions. The spectral equation for these problems is of the form

$$\sin(\xi+\phi_0)=\sum_{j=1}^{K} C_j \sin(\omega_j \xi+\phi_j), \tag{138}$$

where ϕ_0, C_j, ω_j, and ϕ_j are constants, and K is finite if the number of steps (δ functions) is finite. Without tunneling the constants are real. If in addition

$$\sum_{j=1}^{K} |C_j| < 1, \tag{139}$$

the theory developed in Sec. III can be applied and yields explicit periodic-orbit expansions for the roots ξ_n of the spectral equation (138) [20–22]. In the presence of tunneling some, or all, of the ω_j in Eq. (138) become complex. But the theory developed in Secs. III and IV stays applicable as long as

$$\sum_{j=1}^{K} |C_j \sin(\omega_j \xi+\phi_j)| < 1, \quad \text{for all } \xi. \tag{140}$$

Even if Eq. (139) is violated, there already exists the method presented in Ref. [21] to obtain, at least in principle, explicit periodic-orbit expansions for the solutions ξ_n of Eq. (138). We will be able to solve all one-dimensional quantum problems consisting of piecewise constant potentials and δ functions if we can find a method to deal with cases in which the condition (140) is violated. Such a method does not yet exist, and this provides the last road block on the way to solving all one-dimensional quantum problems consisting of piecewise constant potentials and δ-function potentials. Nevertheless, the set of one-dimensional problems that can already be solved via explicit periodic-orbit expansions is large: In addition to the finite square well [42] and the tunneling problem solved here, it contains at least all 1D piecewise constant potentials without tunneling and all δ-function arrays where the δ strengths are positive.

Section IV proposed an experiment for the extraction of ghost orbit information from measured spectra in the tunneling regime (ghost orbit spectroscopy). The question arises "Why do an experiment, if theory is exact, and any experiment can at best approximate theory?" Reasonable answers can be found in a paper entitled with this question [43]. We add the following.

Theory can be "perfect," viz., exactly 1D or 2D, or …. Real experiments have imperfections, and careful measurements can occasionally isolate unanticipated consequences of these imperfections. An example is the surprising sensitivity to "lid warping" of the experiment reported in Refs. [12,13]. A tiny amount of lid warping introduced "3D-ness" into an otherwise 2D experiment, and it establishes the need for developing a fully three-dimensional (3D) vector theory of ray splitting in electromagnetic systems. This 3D case is not equivalent to the scalar theory used for quantal ray splitting, so such a theory will be new and different. Real experiments, therefore, can provide the stimulus for new theory.

VIII. SUMMARY AND CONCLUSIONS

Tunneling is most important below, but close to the threshold $E=V_0$. Thus ghost orbit spectroscopy is best accomplished with an energy-scaling system where, because of $V_0=vE$ with v a constant, one can remain close to, but below, the tunneling threshold $E=V_0$ for all E. For this reason, our focus in this paper is on a simple model, the energy-scaling, step-in-the-box potential, which illustrates the importance of ghost orbits in systems with tunneling.

Our rigorous derivations show that inclusion of ghost orbits provides exact, convergent periodic-orbit expansions of energy eigenvalues in the tunneling regime. We find that our theory, based on a unitary 2×2 scattering matrix, converges and yields the correct spectral eigenvalues in the tunneling regime, whereas a recently published theory [22], based on a nonunitary 4×4 matrix, diverges, and yields incorrect energy eigenvalues in the tunneling regime [28]. The transition from the nonunitary 4×4 theory to the unitary 2×2 theory amounts to a consistent summation of ghost orbits in the two

closed channels of the step-in-the-box potential.

We develop a procedure that allows us to extract ghost orbit information from computed or measured spectra (ghost orbit spectroscopy), and we propose an experiment that implements the scaling, step-in-the-box potential. It will allow measurement of scaled microwave spectra in the tunneling regime. Although it has novel features, such as a frequency-coupled width and a dielectric region with variable width, our proposed experiment is feasible. Measuring on the order of 30 scaled TM_{n10} microwave resonances will provide a clear signal in the (regularized) Fourier transform of the density of resonances to (i) uncover the signature of periodic ghost orbits in the microwave spectra and (ii) measure their (complex) actions.

Finally, we point out that our theory amounts to an exact resummation of Feynman's path integral [44]. According to Feynman, we have to sum over all possible paths in the potential to obtain exact results for the spectral eigenvalues. While this is certainly correct, we show in this paper that the subset of Feynman paths consisting of Newtonian orbits and non-Newtonian ghost orbits is sufficient for obtaining exact results. All the "extra" Feynman paths sum to zero.

ACKNOWLEDGMENTS

A.S.B. and R.B. are grateful for financial support from NSF Grant No. PHY-9984075. P.M.K. was partially supported by NSF Grant No. PHY-0099398.

[1] H. Poincaré, *New Methods of Celestial Mechanics*, edited by D. L. Goroff (American Institute of Physics, Melville, NY, 1993), Vol. 1.
[2] M. C. Gutzwiller, J. Math. Phys. **12**, 343 (1971).
[3] M. C. Gutzwiller, *Chaos in Classical and Quantum Mechanics* (Springer, New York, 1990).
[4] N. L. Balazs and A. Voros, Phys. Rep. **143**, 109 (1986).
[5] J. Keating, The Riemann Zeta-Function and Quantum Chaology in *Quantum Chaos*, edited by G. Casati, I. Guarneri, and U. Smilansky (North-Holland, Amsterdam, 1993).
[6] T. Kottos and U. Smilansky, Phys. Rev. Lett. **79**, 4794 (1997).
[7] T. Kottos and U. Smilansky, Ann. Phys. (N.Y.) **274**, 76 (1999).
[8] L. Couchman, E. Ott, and T. M. Antonsen, Jr., Phys. Rev. A **46**, 6193 (1992).
[9] R. Blümel, T. M. Antonsen, Jr., B. Georgeot, E. Ott, and R. E. Prange, Phys. Rev. Lett. **76**, 2476 (1996).
[10] R. Blümel, T. M. Antonsen, Jr., B. Georgeot, E. Ott, and R. E. Prange, Phys. Rev. E **53**, 3284 (1996).
[11] R. E. Prange, E. Ott, T. M. Antonsen, Jr., B. Georgeot, and R. Blümel, Phys. Rev. E **53**, 207 (1996).
[12] C. Vaa, P. M. Koch, and R. Blümel, Phys. Rev. Lett. **90**, 194102 (2003).
[13] C. Vaa, P. M. Koch, and R. Blümel, Phys. Rev. E **72**, 056211 (2005).
[14] L. Sirko, P. M. Koch, and R. Blümel, Phys. Rev. Lett. **78**, 2940 (1997).
[15] R. Blümel, Acta Physiol. Pol. **A93**, 7 (1998).
[16] K. Karremans, W. Vassen, and W. Hogervorst, Phys. Rev. A **60**, 4764 (1999).
[17] Th. Bartsch, J.Main, and G.Wunner, Phys. Rev. A **66**, 033404 (2002).
[18] D. Delande, K. T. Taylor, M. H. Halley, T. van der Veldt, W. Vassen, and W. Hogervorst, J. Phys. B **27**, 2771 (1994).
[19] M. Kuś, F. Haake, and D. Delande, Phys. Rev. Lett. **71**, 2167 (1993).
[20] R. Blümel, Yu. Dabaghian, and R. V. Jensen, Phys. Rev. Lett. **88**, 044101 (2002).
[21] Yu. Dabaghian and R. Blümel, Phys. Rev. E **70**, 046206 (2004).
[22] Yu. Dabaghian and R. Jensen, Eur. J. Phys. **26**, 423 (2005).
[23] A. S. Bhullar, R. Blümel, and P. M. Koch, J. Phys. A **38**, L563 (2005).
[24] H.-J. Stöckmann, *Quantum Chaos: An Introduction* (Cambridge University Press, Cambridge, 1999).
[25] M. Keeler and T. J. Morgan, Phys. Rev. Lett. **80**, 5726 (1998).
[26] R. Blümel, P. M. Koch, and L. Sirko, Found. Phys. **31**, 269 (2001).
[27] E. Ott, *Chaos in Dynamical Systems* (Cambridge University Press, Cambridge, 1993).
[28] R. Blümel, Eur. J. Phys. **27**, L1 (2006).
[29] A. Messiah, *Quantum Mechanics* (North-Holland, Amsterdam, 1961).
[30] C. Cohen-Tannoudji, B. Diu, and F. Laloë, *Quantum Mechanics*, 3rd ed. (Pergamon Press, Oxford, 1977).
[31] I. S. Gradshteyn and I. M. Ryzhik, *Table of Integrals, Series, and Products*, 5th ed., edited by A. Jeffrey (Academic Press, Boston, 1994).
[32] R. Blümel and Yu. Dabaghian, J. Math. Phys. **42**, 5832 (2001).
[33] J. Riordan, *An Introduction to Combinatorial Analysis* (Wiley, New York, 1958).
[34] *Handbook of Mathematical Functions*, edited by M. Abramowitz and I. A. Stegun (National Bureau of Standards, Washington, DC, 1964).
[35] R. Courant, *Differential and Integral Calculus* (Interscience, New York, 1937).
[36] H.-J. Stöckmann and J. Stein, Phys. Rev. Lett. **64**, 2215 (1990).
[37] J. D. Jackson, *Classical Electrodynamics* (John Wiley, New York, 1975).
[38] *Handbook of Chemistry and Physics*, 55th ed., edited by R. C. Weast (CRC Press, Cleveland, Ohio, 1974).
[39] S. Sridhar, Phys. Rev. Lett. **67**, 785 (1991).
[40] S. Sridhar, D. O. Hogenboom, and B. A. Willemsen, J. Stat. Phys. **68**, 239 (1992).
[41] N. Savytskyy, A. Kohler, Sz. Bauch, R. Blümel, and L. Sirko, Phys. Rev. E **64**, 036211 (2001).
[42] R. Blümel, J. Phys. A **38**, L673 (2005).
[43] H.-J. Stöckmann, Phys. Scr. **T90**, 246 (2001).
[44] R. P. Feynman, Rev. Mod. Phys. **20**, 367 (1948).